PHYSICAL REVIEW D VOLUME 38, NUMBER 7 1 OCTOBER 1988

High-precision measurement of polarized-Σ^- beta decay

S. Y. Hsueh,* D. Müller, J. Tang, R. Winston, and G. Zapalac†
Enrico Fermi Institute, The University of Chicago, Chicago, Illinois 60637

E. C. Swallow
Department of Physics, Elmhurst College, Elmhurst, Illinois 60126
and Enrico Fermi Institute, The University of Chicago, Chicago, Illinois 60637

J. P. Berge, A. E. Brenner,‡ P. S. Cooper, P. Grafström,§ E. Jastrzembski,** J. Lach,
J. Marriner, R. Raja, and V. J. Smith††
Fermi National Accelerator Laboratory, Batavia, Illinois 60510

E. McCliment and C. Newsom
Department of Physics, University of Iowa, Iowa City, Iowa 52442

E. W. Anderson
Department of Physics, Iowa State University, Ames, Iowa 50011

A. S. Denisov, V. T. Grachev, V. A. Schegelsky, D. M. Seliverstov, N. N. Smirnov, N. K. Terentyev,
I. I. Tkatch, and A. A. Vorobyov
Leningrad Nuclear Physics Institute, Leningrad, Union of Soviet Socialist Republics

P. Razis‡‡ and L. J. Teig§§
J. W. Gibbs Laboratory, Yale University, New Haven, Connecticut 06511

(Received 22 January 1988)

We report the results of a polarized-Σ^- beta-decay experiment carried out in the Fermilab Proton Center charged-hyperon beam. These results are based on 49 671 observed $\Sigma^- \rightarrow n e^- \bar{\nu}$ decays. The Σ^- beam had a nominal momentum of 250 GeV/c and was produced by 400-GeV/c protons impinging on a Cu target. At a production angle of 2.5 mrad, the polarization was (23.6±4.3)%. The decay asymmetries of the electron ($\alpha_e = -0.519 \pm 0.104$), neutron ($\alpha_n = +0.509 \pm 0.102$), and antineutrino ($\alpha_\nu = -0.230 \pm 0.061$) were measured and used to establish sign and approximate magnitude of the axial-vector-to-vector form-factor ratio g_1/f_1. The form-factor ratios $|g_1/f_1|$ and f_2/f_1 were determined most sensitively from the neutron and electron center-of-mass spectra, respectively. We obtain $|g_1/f_1 - 0.237 g_2/f_1| = 0.327 \pm 0.007 \pm 0.019$ and $f_2(0)/f_1(0) = -0.96 \pm 0.07 \pm 0.13$, where the stated errors are statistical and systematic, respectively. A general fit that includes the asymmetries and makes the conventional assumption $g_2 = 0$ gives the final value $g_1(0)/f_1(0) = -0.328 \pm 0.019$. The data are also compatible with positive values for g_2/f_1 combined with corresponding reduced values for $|g_1/f_1|$.

I. INTRODUCTION

Baryon semileptonic decays are commonly described by the Cabibbo model[1] which assumes that the hadronic weak vector (V) and axial-vector (A) currents belong to SU(3) octets, and that the leptonic current is left handed. It has long been recognized[2] that the prediction of a *negative* sign for the axial-vector-to-vector form-factor ratio g_1/f_1 in $\Sigma^- \rightarrow n e^- \bar{\nu}$ (i.e., *opposite* to the *positive* sign observed in neutron beta decay and in other strangeness-changing beta decays) is a major characteristic feature of this model. The unambiguous determination of this sign therefore provides a crucial qualitative test of the model. At a more detailed level, assuming exact SU(3) symmetry, the Cabibbo model provides a description of all octet baryon beta decays in terms of SU(3) Clebsch-Gordan coefficients and a few free parameters (reduced form factors and the Cabibbo angle).

Determinations of g_1/f_1 for other decays are in reasonable agreement[3,4] with this picture. On the other hand, four previous experiments[5-8] with polarized Σ^- failed to confirm[9] the predicted negative sign for g_1/f_1 in $\Sigma^- \rightarrow n e^- \bar{\nu}$. Small sample sizes, substantial background levels, and limited control of the Σ^- polarization were clear limitations of these early low-energy experiments.

Experiments with unpolarized Σ^- are primarily sensitive to the absolute value $|g_1/f_1|$. With one exception,[10] such experiments have been in reasonable agreement with each other[11-15] and with the Cabibbo model. The most recent[15] of these attempted to infer the sign of g_1/f_1 from the electron spectrum. This analysis favored a negative sign. However, the sensitivity to g_1/f_1 is quite small (the spectrum shape is dominated by phase space) and highly dependent on radiative corrections and the assumed value for the weak-magnetism form factor f_2. A decisive experimental result was certainly needed to clarify this situation. The experiment reported here was undertaken to provide it.

This experiment was performed using the Fermilab Proton Center charged-hyperon beam. This facility is a powerful tool for the study of hyperon physics since polarized hyperons (particularly Σ^-) are produced copiously, and their direction of polarization can be easily changed. We employed double electron identification to distinguish the rare beta-decay mode, $\Sigma^- \to n e^- \bar{\nu}$, from the dominant decay mode $\Sigma^- \to n\pi^-$. The momenta of the Σ^-, electron, and neutron were individually measured thus allowing full reconstruction of the decay. Because the Σ^- were produced polarized, we were able to measure the electron, neutron, and antineutrino asymmetries (α_e, α_n, and α_ν). The electron and neutron spectra in the Σ^- rest frame were also analyzed. Results reported here are based on a sample of 49 671 Σ^- beta-decay events with 2% background. A preliminary value of α_e based on a subsample of this data was published previously.[16] This paper supersedes it.

II. THEORY AND NOTATION

For the semileptonic decay $\Sigma^- \to n e^- \bar{\nu}$, the matrix element can be written as

$$M = \frac{G}{\sqrt{2}} \langle n \mid J^\mu \mid \Sigma^- \rangle \bar{u}(e^-)\gamma_\mu(1+\gamma_5)u(\nu) \ , \qquad (2.1)$$

where G is the universal weak coupling constant. The hadronic current can be written in terms of three vector form factors, f_1 (vector), f_2 (weak magnetism), and f_3 (induced scalar), and three axial-vector form factors, g_1 (axial vector), g_2 (induced pseudotensor or weak electricity), and g_3 (induced pseudoscalar):

$$\langle n \mid J^\mu \mid \Sigma^- \rangle = \sin\theta_C \bar{u}(n) \left[f_1(q^2)\gamma^\mu + \frac{f_2(q^2)}{M_{\Sigma^-}}\sigma^{\mu\nu}\gamma_\nu + \frac{f_3(q^2)}{M_{\Sigma^-}} q^\mu + \left[g_1(q^2)\gamma^\mu + \frac{g_2(q^2)}{M_{\Sigma^-}}\sigma^{\mu\nu}\gamma_\nu + \frac{g_3(q^2)}{M_{\Sigma^-}} q^\mu \right] \gamma_5 \right] u(\Sigma^-) \ . \qquad (2.2)$$

Here θ_C is the Cabibbo angle, u is a Dirac spinor, and q^2 is the momentum transfer squared between Σ^- and the neutron. The six form factors are functions of q^2 and, unless explicitly noted otherwise, we discuss their values at $q^2=0$. Contributions to the decay distributions from f_3 and g_3 are proportional to the electron mass divided by the baryon mass and are therefore set to zero. We follow the calculation and use the notation of Garcia and Kielanowski.[17]

According to the Cabibbo model, the form factors for the baryon-octet semileptonic decays are related to each other by SU(3) Clebsch-Gordan coefficients. For Σ^- beta decay in the SU(3)-symmetry limit, $f_1(0) = -1$ and $f_2(0)/M_{\Sigma^-} = -(\mu_p + 2\mu_n)/2M_p$, where μ_n and μ_p are, respectively, the neutron and proton anomalous magnetic moments in units of nuclear magnetons. Taking[18] $\mu_p = 1.793$ and $\mu_n = -1.913$, we get $f_2(0)/f_1(0) = -1.30$ in the SU(3) limit.[19] The form factor g_1 for $\Sigma^- \to n e^- \bar{\nu}$ is given by the difference of two reduced form factors D and F. These represent the symmetric and antisymmetric coupling, respectively, of two SU(3) octets to form a third. A recent fit[3,20] to the Cabibbo model gave $F = 0.477 \pm 0.012$ and $D = 0.756 \pm 0.011$ corresponding to $g_1/f_1 = F - D = -0.279 \pm 0.023$ for the decay $\Sigma^- \to n e^- \bar{\nu}$. The g_2 form factor is due to a second-class current and thus is zero in the SU(3) limit.

Next we consider the effects of SU(3)-symmetry breaking. The Ademollo-Gatto theorem[21] implies that, to first order in $\epsilon = (M_{\Sigma^-} - M_n)/M_{\Sigma^-}$, f_1 is not renormalized. In the same spirit, Sirlin[22] has shown that, to first order in symmetry breaking,

$$f_2(0)/M_{\Sigma^-} = \frac{1}{2M_p}[\mu_{\Sigma^-} - \mu_n + (\mu_{\Sigma^+} - \mu_p)/2] \ . \qquad (2.3)$$

The μ's are anomalous magnetic moments in units of nuclear magnetons. With current values of the magnetic moments,[23,18] $\mu_{\Sigma^-} = -0.385 \pm 0.024$ and $\mu_{\Sigma^+} = 1.59 \pm 0.02$, this expression yields $f_2(0) = 0.910 \pm 0.034$. We note that in the SU(3)-symmetry limit, Eq. (2.3) becomes $-(\mu_p + 2\mu_n)/(2M_p)$ yielding $f_2(0) = 1.30$.

Various attempts have been made to calculate QCD corrections to the axial-vector g_1 form factor.[24] Recent calculations[25–27] give results that agree well with each other and in fact, depart only slightly from the SU(3) value (see Table I).

The g_2 term is expected to be nonzero given that SU(3) is broken. It is expected to be proportional to $\Delta m/m$ where m is a quark mass and Δm is a quark-mass difference (between the strange and down quarks in our case). In fact, it has been shown[28] explicitly that the gluon-exchange correction to the quark decay vertex indeed induces a g_2 term proportional to $\Delta m/m$. The same authors have also argued that the confinement of quarks reduces the induced g_2 term. These two competing mechanisms have been evaluated[27] recently in the context of a bag model. Other authors[29–31] have calculated g_2 using various bag models. These g_2 calculations

TABLE I. Theoretical predictions for $\Sigma^- \rightarrow n e^- \bar{\nu}$ form factors.

Form factor	SU(3) exact	SU(3) broken
$f_1(0)$ vector	-1 (Ref. 1)	-1 (Ref. 21)
$f_2(0)$ weak magnetism	1.30 (Ref. 19)	0.910±0.034 (Ref. 22)
$f_3(0)$ induced scalar	Contribution to the matrix element $\approx M_e/M_\Sigma \Longrightarrow 0$	
$g_1(0)$ axial vector	0.279±0.023 (Ref. 3)	0.31 (Ref. 25) 0.29 (Ref. 27) 0.31 (Ref. 29)
$g_2(0)$ weak electricity	0.0	-0.021 (Ref. 27) 0.46 (Ref. 29) -0.022 (Ref. 30) -0.10 (Ref. 31)
$g_3(0)$ induced pseudoscalar	Contribution to the matrix element $\approx M_e/M_\Sigma \Longrightarrow 0$	

are summarized in Table I.

In Eq. (2.2) we can factor out f_1. Experimentally this means that, unless the total rate is measured and $\sin\theta_C$ is known, only the ratios f_2/f_1, g_1/f_1, and g_2/f_1 can be determined. The assumption of time-reversal symmetry constrains these ratios to be real.

The q^2 dependence[32] of the form factors is assumed to be

$$f_1(q^2)=f_1(0)(1+2q^2/M_V^2)\ ,$$
$$g_1(q^2)=g_1(0)(1+2q^2/M_A^2) \tag{2.4}$$

with $M_V=0.97$ GeV/c^2 and $M_A=1.25$ GeV/c^2. The choice of the pole masses is discussed in Ref. 3. Our results are insensitive to the q^2 dependence of f_2 and g_2.

The decay product angular distributions in the center of mass (c.m.) of the Σ^- for each of the decay particles, electron, neutron, and antineutrino can be expressed as

$$\frac{dN}{d\Omega}=\frac{N}{4\pi}(1+\alpha\mathbf{P}\cdot\boldsymbol{\omega})\ . \tag{2.5}$$

Here α is the pertinent asymmetry parameter, $\mathbf{P}$ is the Σ^- polarization vector, N is the total number of events, and $\boldsymbol{\omega}$ is a unit vector in the direction of solid-angle element $d\Omega$.

Differential decay rates and α_i's have been calculated by several authors.[17,33–35] The complete formulas used in our analysis are tedious and thus are not reproduced here, but they can be found on pp. 12–15 of Ref. 17. Radiative corrections are also included in our analysis. We have used the expressions of Töth, Margaritisz, and Szegö.[36,37] The calculations include the effects of virtual-photon exchange as well as the real-photon process $\Sigma^- \rightarrow n e^- \bar{\nu}\gamma$.

III. EXPERIMENTAL APPARATUS AND TRIGGER

A. Overview

A plan view of the experiment is shown in Fig. 1. Our coordinate system is defined with the positive y axis in the vertical direction, the z axis along the beam, and the x axis in the direction forming a right-handed system.

Because the Σ^- beta-decay branching ratio is $\approx 10^{-3}$, our central design requirement was to have good e/π discrimination to distinguish $\Sigma^- \rightarrow n e^- \bar{\nu}$ from $\Sigma^- \rightarrow n\pi^-$ events, while maintaining high electron efficiency. To accomplish this, both a transition-radiation detector (TRD) and a lead-glass calorimeter (LGC) were used to identify electrons.

Equally important was the ability to reverse the polarization of the Σ^- beam. The electron (neutron, antineutrino) asymmetry is measured by comparing the number of electrons (neutrons, antineutrinos) emitted in the same direction as the polarization with the number emitted opposite to the direction of the Σ^- polarization. Limited acceptance and efficiency of detectors makes a bias-free comparison difficult. Reversing the Σ^- polarization allows us to reverse the preference of electrons (neutrinos, antineutrinos) without changing the acceptance and efficiency of the apparatus. This experiment measured the asymmetries by comparing two data samples with opposite polarizations. The symmetry of the apparatus combined with its high efficiency minimized our experimental biases. Residual experimental biases were, to an excellent approximation, canceled by comparing the two sets of data. The experiment was not designed to deter-

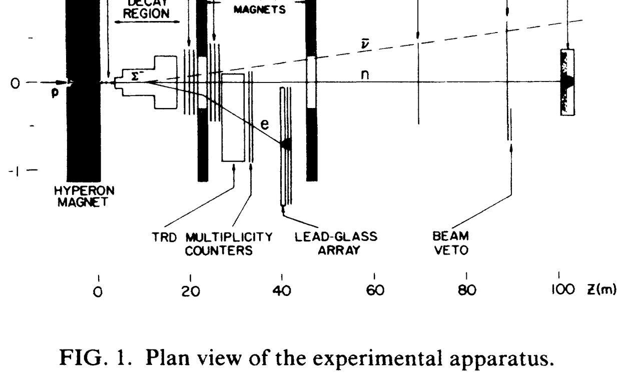

FIG. 1. Plan view of the experimental apparatus.

mine the Σ^- decay rate or the $\Sigma^- \to n e^- \bar{\nu}$ branching ratio.

The Σ^- polarization was measured using $\Sigma^- \to n \pi^-$ decays since the π^- asymmetry parameter α_π is known[18] to be 0.068±0.008. Two-body-decay data were recorded simultaneously with $\Sigma^- \to n e^- \bar{\nu}$ data. The asymmetry $(\alpha_\pi P)$ was determined using the same bias canceling technique.

The source of Σ^- particles was a momentum selected charged secondary beam produced by 400-GeV/c protons incident on a Cu target. In order to reconstruct the decay completely, the momenta of the Σ^-, electron, and neutron were measured. The momentum of the antineutrino was calculated using momentum conservation. The trajectories of the Σ^- and electron were measured by wire chambers. A calorimeter was used to measure the neutron energy. The neutron impact point in the calorimeter was also measured, thus allowing us to determine the direction of neutron momentum.

Our data were collected over a period of five months. We recorded 40×10^6 triggers on 400 magnetic tapes; the data for each trigger were contained in 350 16-bit words. Polarization was reversed regularly throughout the run. About one-fifth of the data was taken at nominally zero polarization. The unpolarized data sample was useful in studying effects of possible instrumental bias and also contributed to the decay spectrum analysis.

B. Charged-hyperon beam

We performed the experiment in the Proton Center charged-hyperon beam at Fermilab. The 400-GeV/c primary proton beam from the Fermilab Tevatron impinged upon a Cu target (0.2×0.2 cm^2 in cross section and 14.3 cm in the beam direction) to produce a 250-GeV/c charged-hyperon secondary beam[38] (Fig. 1). During data taking, we normally targeted 3×10^{11} protons per 15-sec beam pulse which was repeated every 39 sec. Secondary beam particles were collimated by a curved tungsten channel embedded in a 7.3-m-long magnet,[38] the hyperon magnet, which was set to deflect 250-GeV/c charged particles by 21 mrad. At the channel exit, the beam had a momentum spread $\Delta p / p = 14\%$ (full width measured at the base of the distribution) and subtended a solid angle of 0.64 μsr. The beam composition[38] at the exit of the hyperon channel was about 10% Σ^-, 0.5% Ξ^-, and the rest mostly π^-.

Polarized Σ^- were produced by steering the primary proton beam to hit the target at an angle relative to the direction of the Σ^- secondary beam. Parity conservation in the production process requires that any polarization be normal to the production plane defined by the two beam directions. We use the usual convention that a positive hyperon polarization is in the direction of $\mathbf{p}_p \times \mathbf{p}_\Sigma$. The sign of the polarization is changed by reversing the targeting angle. We alternated the nominal targeting angles in the sequence +3, −3, 0, −3, and +3 mrad. Actual measured angles are tabulated in Table II. The uncertainties in all targeting angles are about 0.14 mrad. [Unless otherwise noted all quoted uncertainties are one standard deviation (σ).]

The data reported here were separated into two sets: horizontal targeting (θ_h) and vertical targeting (θ_v). The θ_h (θ_v) data were taken when the proton beam was directed to hit the target at an angle in the x-z (y-z) plane. The allowed polarization at production is then in the y (x) direction. Since the magnetic field in the hyperon magnet was in the vertical direction, the Σ^- polarization vector for horizontal targeting was unaffected by the field. For vertical targeting, the Σ^- polarization vector was perpendicular to the field and therefore precessed in the hyperon magnet. Thus the Σ^- polarization at the channel exit was in the x-z plane. In another portion of this experiment, its orientation was used to measure the Σ^- magnetic moment.[23]

C. Momentum measurements

Trajectories of Σ^- particles were measured by a set of 12 high-pressure proportional wire chambers (PWC's) (Ref. 39) after the channel exit. Momenta of charged decay particles (e^- or π^-) were measured by a spectrometer consisting of six drift-chamber (DC) clusters of three planes each with wires oriented in the x, y, and u (45°) direction. Each spectrometer magnet (Fig. 1) imparted a transverse momentum (p_t) of about 0.8 GeV/c. For this analysis the second spectrometer magnet served only to deflect charged particles away from the neutron detector.

Between the PWC's and the upstream drift chambers was a partially evacuated 14.43-m-long decay region.

TABLE II. Summary of targeting angles, hyperon momenta, and proton beam positions for our six data samples.

Nominal angle (mrad)	Actual angle (mrad)	Average momentum (GeV/c)	Beam position (x_T) (cm)
		Horizontal	
+3	2.10	237.5	−0.136
0	−0.54	243.3	−0.089
−3	−3.06	253.5	0.0
		Vertical	
+3	3.07	244.7	−0.067
0	0.74	244.7	−0.067
−3	−2.01	244.7	−0.067

This decay region contained ≈10 Torr of nitrogen gas and was used as a threshold Cherenkov counter to tag beam electrons for calibration purposes.

The PWC system provided single-plane resolution of 60 μm and beam-track angular resolution of 25 μrad. Taking into account the proton beam size at the target (approximately ± 1 mm), the momentum resolution for beam particles was $\Delta p/p = 0.7\%$.

Our DC momentum resolution was $\Delta(1/p) = 0.0004$ $(\text{GeV}/c)^{-1}$. The angular resolution was 150 μrad in azimuth and 50 μrad in dip which is small compared to the typical 3-mrad π^- decay angle of $\Sigma^- \rightarrow n\pi^-$.

The hyperon magnet and the curved channel embedded in it bend the secondary beam in the x-z plane. We parametrize the field of the hyperon magnet by the momentum of a particle that originates from the center of the target and follows the curvature of the channel. Particles with a different curvature have a momentum given by $1/p = (1 - \rho_c \Delta)/p_c$, where p_c and ρ_c are the central ray momentum and channel radius of curvature and Δ is the curvature of the particle orbit relative to the central ray. To calculate the Σ^- momentum from the PWC data we also needed to know the average x coordinate (x_T) of the incident proton beam at the target.

The determination of p_t for the upstream spectrometer magnet (Fig. 1) and p_c and x_T of the hyperon magnet was done in two steps. First, we assumed that the target position of the $\theta_h = -3$ mrad data was at the center of the channel $(x_T = 0)$. This assumption was justified because the $\theta_h = -3$ mrad beam phase space was fully populated and in good agreement with our Monte Carlo simulation. Then the central ray momentum p_c of the hyperon magnet and p_t of the upstream spectrometer magnet were determined by requiring that $\Sigma^- \rightarrow n\pi^-$ events gave the correct reconstructed Σ^- mass independent of decay angle.

Since the currents in the hyperon magnet and the spectrometer magnets were the same for all targeting angles, in step 2 we took p_c and p_t to be the same for all of the data sets. Using the values determined from the $\theta_h = -3$ mrad data, we then determined x_T for each of the other data sets.

The $\Xi^- \rightarrow \Lambda\pi^-$ reconstructed mass can be used as an additional constraint to check the calibration. The three constraints (Σ^- mass, decay angle independence, and Ξ^- mass) determined the three calibration constants (x_T, p_c, and p_t) uniquely.

As an additional check, nondecaying beam tracks were recorded simultaneously with the data taking. These were used to verify the target position.

Note that the vertical target position, unlike the horizontal target position, can be calculated event by event. It was used to cut events not from the target. This cut is discussed in Sec. V B.

The sensitivity of this calibration procedure to p_t is about 1 MeV/c^2 in Σ^- mass per 1% change in p_t. The sensitivity to x_T and p_c are 0.024 cm and 1 GeV/c per 1 MeV/c^2, respectively. The values of x_T and average beam momentum for each targeting angle are shown in Table II.

D. Electron-identification detectors

Two detector systems were used to identify electrons from semileptonic decays: a transition-radiation detector (TRD) and a lead-glass calorimeter (LGC).

The TRD (Refs. 40 and 41) consisted of 12 identical modules, each containing a radiator followed by a multiwire proportional chamber (MWPC) (Fig. 2). The radiator had 210 sheets of 17-μm polypropylene separated by 1.0-mm air gaps. Each MWPC had an active area of 0.6×1.0 m^2 and was filed with a Xe-CH$_4$ mixture for efficient x-ray detection. Downstream of the TRD detector was a set of four scintillator counters (MC, "multiplicity counters" in Fig. 1) used to identify interactions in or before the TRD on the basis of charged-particle multiplicities (Fig. 3).

While transition-radiation x rays produce ionization in only a small portion of the chamber gap, penetrating charged particles produce ionization spread throughout the gap. The cluster counting technique,[42] which took advantage of this difference, was used (both on line in our trigger and off line in our analysis) to identify electrons traversing the TRD.

The LGC consisted of a 3.4-radiation-length (r.l.) sheet of lead followed by an array of 72 type SF-5 lead-glass blocks[43] (each $15 \times 15 \times 45$ cm^3) arranged in four up-down symmetric layers (Fig. 4). Each layer had a sensitive area of 1.35×0.90 m^2 and a thickness of 6.37 r.l. Behind the array was a lead brick wall. Electromagnetic showers which developed in the LGC were completely absorbed by this wall, while typical hadronic showers reached their maximum intensity near the back of the wall.

Plastic scintillation counters were installed in front of the lead sheet, between it and the array (LGS1), between the layers of the array, and behind the lead wall (LGS5). LGS1 and LGS5 were used in the off-line analysis; the other scintillators were used only for setup and monitoring. The signal from LGS1 was included in the calculation of the total energy deposited in the LGC. Signals from LGS5 were used to reject hadronic-shower events off line.

The energy deposited in LGC was calculated by com-

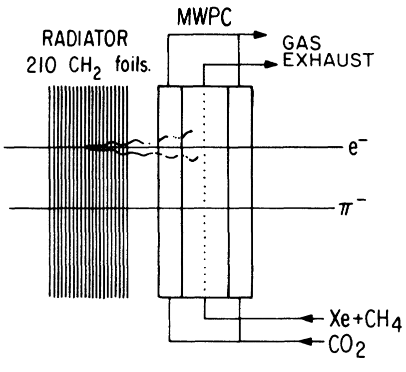

FIG. 2. One of the 12 modules of the TRD system. The transition-radiation x rays produced when an electron passes through the radiator are detected by the MWPC.

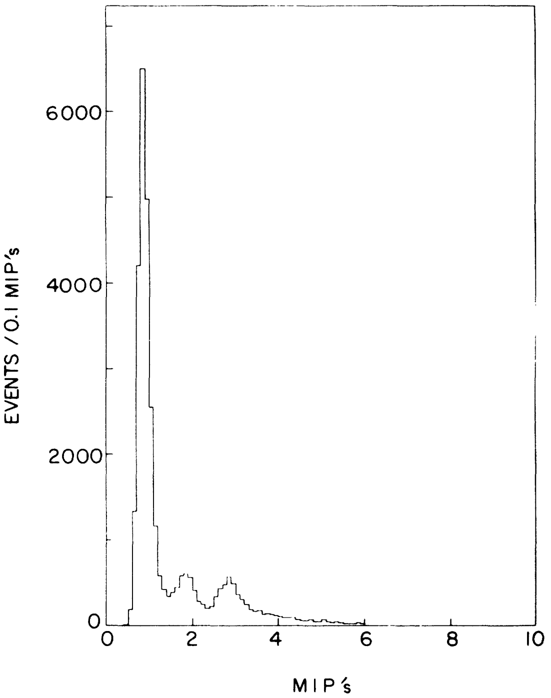

FIG. 3. The summed-pulse-height distribution for the four multiplicity counters (Fig. 1). These were used to reject interactions in the upstream portion of the apparatus, especially in the TRD. The horizontal scale is in units of minimum-ionizing particles (MIP's).

bining the (properly normalized) signal from LGS1 with signals from the three stacks (12 blocks) nearest the electron impact point as determined from the DC trajectory. If the impact point was within 5 cm of the midplane, both top and bottom stacks (24 blocks) were summed. Events with impact points less than 5 cm from the top, bottom, or sides of the array were eliminated by a fiducial cut.

The LGC gains were monitored with light from two sources: (a) light-emitting diodes attached to each block and (b) light from a central Xenon flash lamp distributed by optical fiber cables to each block. Similar monitoring was also employed for the neutron calorimeter.

E. Electron-beam calibration

An important feature of this experiment was our ability to perform *in situ* calibration and monitoring of our electron detectors with an electron beam. By decreasing the hyperon magnet current, we obtained secondary beams which were rich in electrons (10% at 30 GeV/c) with momenta comparable to those in detected beta-decay events. The decay pipe (Fig. 1), located between the PWC and DC regions, was filled with ≈ 10 Torr of nitrogen gas and instrumented with a spherical mirror and photomultiplier tube. It was used as a threshold Cherenkov counter to identify electrons in the calibration runs. A small dipole magnet (not shown in Fig. 1) located at the beginning of the decay pipe was used to bend the beam vertically.

Identified beam electrons were used to map the efficiency of the TRD (Refs. 40 and 41) and to monitor its performance periodically during the experiment. The average measured (on-line) electron efficiency for the TRD was greater than 99%.

The LGC was mounted so that it could be moved horizontally under remote control. Using a combination of LGC horizontal motion and the vertical bending magnet, a 30-GeV/c beam could be steered to any desired point on the face of the LGC. The absolute calibration of the LGC was established with 30-GeV/c electrons directed onto the center of each stack of blocks. Points above and below the stack center were studied to obtain corrections for spatial nonuniformity of the block response. We also

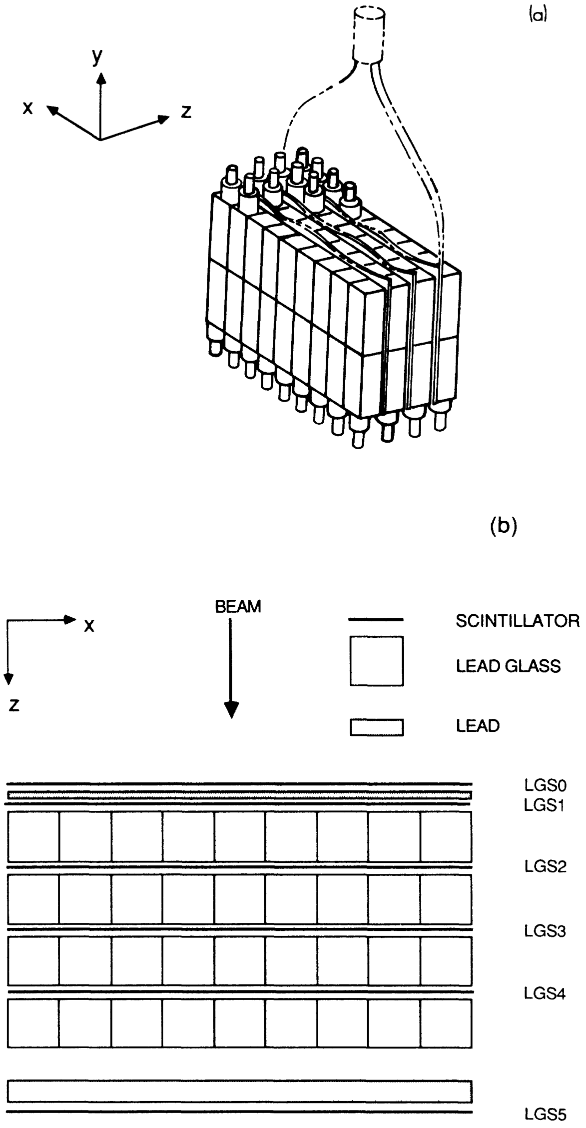

FIG. 4. The lead-glass calorimeter (LGC). (a) The glass blocks were configured in four layers in the z direction counters between the layers. (b) The top view showing the longitudinal geometry of lead, glass, and scintillators. The media type is indicated in upper-right corner.

recorded electron beam data at 10, 20, 30, 40, and 50 GeV/*c* to check the linearity of the LGC and to investigate the momentum dependence of our electron selection criteria in the off-line analysis. The energy resolution of the LGC was determined to be 4.3% [full width at half maximum (FWHM)] at 30 GeV/*c* [Fig. 5(a)]. Its gain was constant to within ±0.2% from 10 to 50 GeV/*c* [Fig. 5(b)]. Note the point at 28 GeV/*c* is higher because the beam hit the crack between the glass blocks. (See also Sec. V B.)

F. Neutron calorimeter

The lead-glass array was followed by a magnet (the second spectrometer magnet of Fig. 1) which swept away charged particles. Neutrons impinged on the neutron calorimeter[44] (NC) at 90.5 m downstream of the average decay vertex allowing precise determination of their energy and direction. The calorimeter (15.2 interaction lengths) comprised 50 Fe plates and scintillator modules (Fig. 6). Between the first 18 plates are interleaved 17 PWC's (NCPWC) to determine the neutron position. The size of both steel plates and scintillators is 0.76×0.76 m^2, while the NCPWC chambers are 0.48×0.48 m^2 and have a wire spacing of 1 cm. $\Sigma^- \rightarrow n\pi^-$ events were used to calibrate the energy and position reconstruction of the neutron. We obtained a 5.3% energy resolution for 200-GeV neutrons and a 1-cm position resolution (Fig. 7).

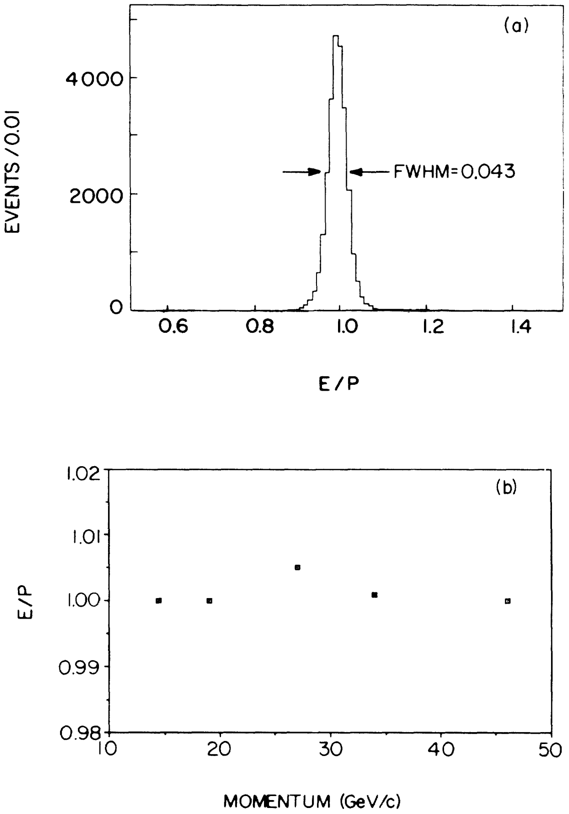

FIG. 5. The LGC energy (a) resolution and (b) linearity. In (a) the E/p distribution for a 30-GeV/*c* e^- beam run is shown. The electron energy E is measured by the LGC and the electron momentum p is determined by the magnetic spectrometer. To illustrate the LGC linearity, we plot in (b) the value of E/p as a function of electron momentum.

It is well known that the apparent energy deposited in the calorimeter by an electromagnetic shower is larger than that from a hadronic shower. If the initial neutron interaction in the calorimeter contains a large fraction of π^0's, the shower will be of electromagnetic nature. The energy measured is sensitive to the fluctuation of the π^0 content. We took advantage of the fact that electromagnetic showers are shorter and have larger pulse heights. For each shower we calculated the second moment of the shower distribution and used it to correct the energy. This correction improved the resolution at 200 GeV by 0.2%.

The most energetic charged shower particles (with the longest trajectories) convey the best information on neutron direction. Accordingly, each hit of the NCPWC was assigned a weight equal to the length of the associated trajectory. At each chamber plane hits were separated into groups and the group with highest weight was selected for calculating position. The shower position at each plane was then calculated as the weighted mean of the group, and the neutron coordinate as the average of shower positions at each plane. We successfully found neutron coordinates for 98% of the events.

G. Triggers

A "beam trigger" was defined by three small scintillation counters in the region of the PWC's (Fig. 1); two additional counters rejected particles outside of the beam region.

A Σ^- "decay trigger" to either the leptonic or hadronic mode required a beam trigger plus at least 20 GeV of energy deposited in the NC, no signal in a scintillation

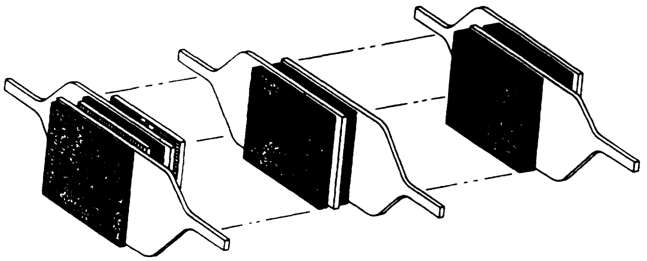

FIG. 6. Schematic drawing of the neutron calorimeter (NC). The calorimeter was divided into three sections. The upstream section has twenty 3.8-cm-thick Fe plates, the middle section twenty-five 5.1-cm Fe plates, the downstream section five 10.2-cm Fe plates. In addition to Fe and scintillator, the upstream section also contained proportional wire chambers.

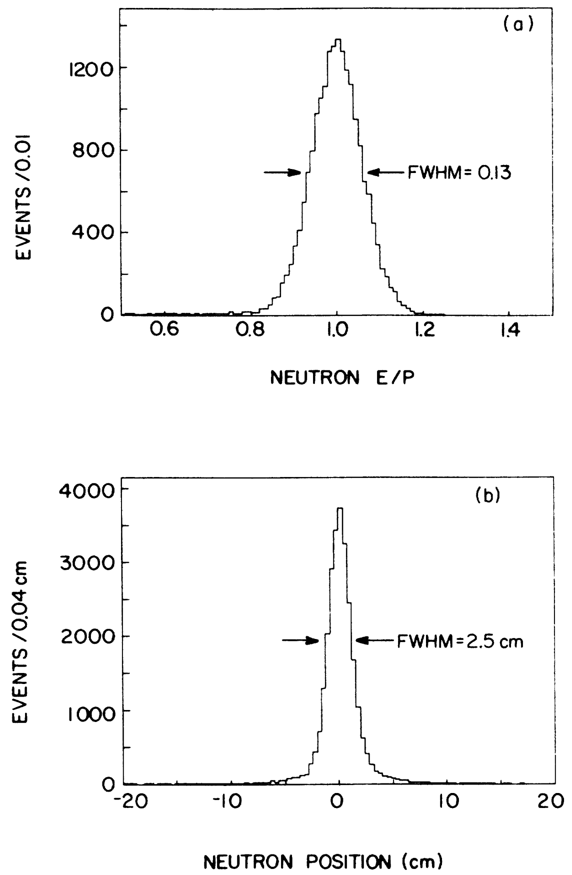

FIG. 7. The neutron-calorimeter (NC) energy and position resolution. In (a) the energy measured by NC divided by the energy predicted from a sample of neutrons from the kinematically constrained decay $\Sigma^- \rightarrow n\pi^-$. For the same event sample we plot in (b) the difference between the neutron x position as measured by the NC and as predicted from the spatial reconstruction of the event.

counter ("neutron veto" in Fig. 1) in front of the NC, and no signal in a scintillation counter which intercepted noninteracting, nondecaying beam particles ("beam veto" in Fig. 1). The neutron veto was sufficiently far upstream so that albedo from the calorimeter was out of time.

A Σ^- "beta-decay trigger" required the above plus a signature in the TRD consisting of 12 or more TRD clusters detected by 7 or more TRD chambers.

IV. MONTE CARLO SIMULATION

A. General description

While our determination of decay asymmetries is, by design, not directly dependent on a detailed Monte Carlo simulation of the experiment, we have nonetheless carried out such a simulation. It proved to be essential for

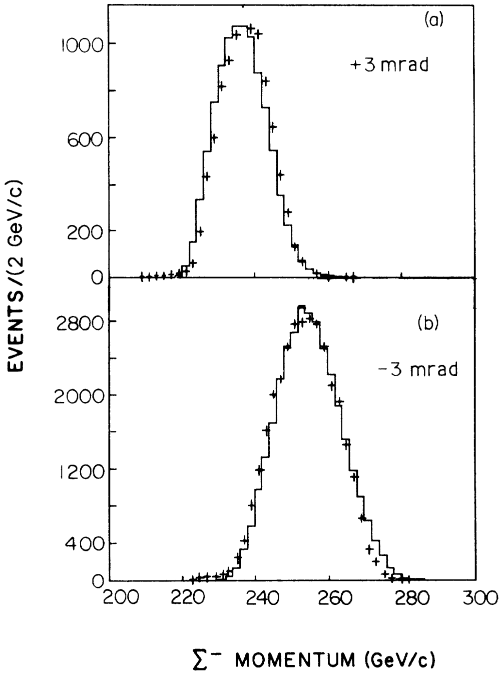

FIG. 8. Comparison of the experimental data (+) and Monte Carlo simulation (—) for Σ^--beam momentum distributions at $\theta_h = +3$ and -3 mrad targeting angles.

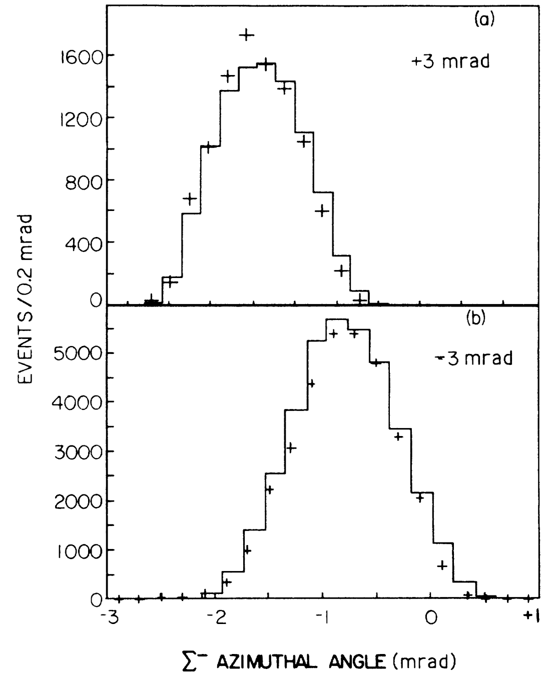

FIG. 9. Comparison of the experimental data (+) and Monte Carlo simulation (—) for Σ^--beam angular distributions (azimuth) in the x-z plane at $\theta_h = +3$ and -3 mrad targeting angles.

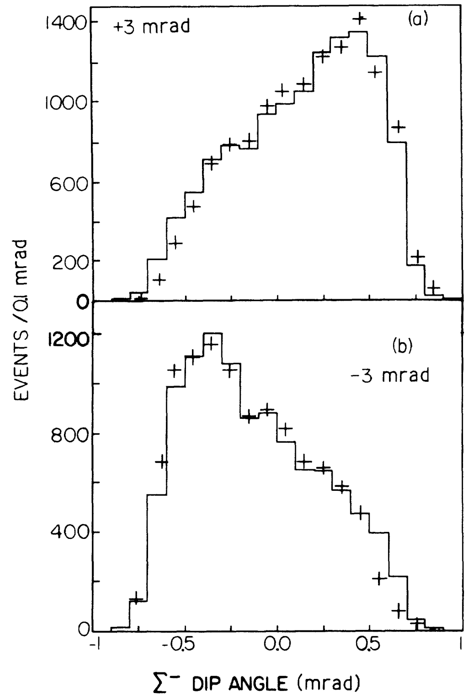

FIG. 10. Comparison of experimental data (+) and Monte Carlo simulation (—) for Σ^--beam angular distributions (dip) in the y-z plane at $\theta_v = +3$ and -3 mrad targeting angles.

our analysis of the electron and neutron spectra in the Σ^- rest frame. For the asymmetry analysis, it also allowed us to evaluate some small corrections and to check the robustness of our bias-canceling technique.

In the Monte Carlo program, beam tracks were generated using the known hyperon magnet channel geometry and transverse momentum dependence of the production process. The central ray momentum (p_c) and target position (x_T) used were determined from the momentum calibration process. The Σ^- hyperons were then tracked through the PWC's. After they decayed, the charged decay products were propagated through the spectrometer magnet and drift chambers. Multiple Coulomb scattering was included for all charged particles including the Σ^-. The material between the decay vertex and the spectrometer magnet was determined to be 0.059±0.002 r.l. Energy loss due to bremsstrahlung was calculated with formulas given in Ref. 45. The direction of the electron was assumed to be unchanged by the bremsstrahlung.

Measured drift times, neutron positions in the calorimeter, and neutron energies were all simulated with Gaussian distributions of known resolution. Each drift chamber was assigned a uniform efficiency. The small residual up-down asymmetry in the TRD was also included in the simulation.

B. Comparison between Monte Carlo simulation and data

Comparison between data and the Monte Carlo simulation are shown in Figs. 8–12. Figures 8 and 9 show the

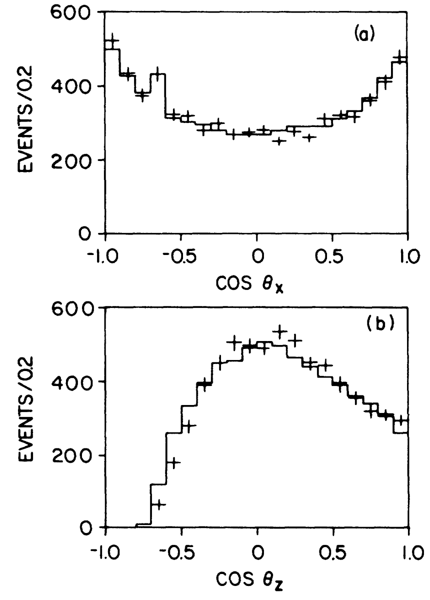

FIG. 11. Comparison of experimental data (+) and Monte Carlo (—) c.m. angular distributions of electrons from the decay $\Sigma^- \rightarrow ne^-\bar{\nu}$ projected onto the (a) x and (b) z axes. Note that our acceptance for backward electrons is quite low.

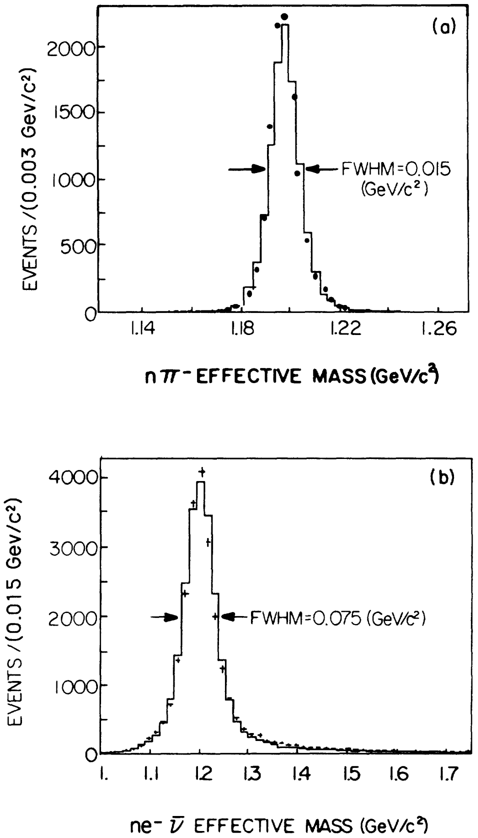

FIG. 12. Comparison of experimental data (+) and Monte Carlo (—) Σ^- effective-mass distributions as determined for the decays (a) $\Sigma^- \rightarrow n\pi^-$ and (b) $\Sigma^- \rightarrow ne^-\bar{\nu}$.

Σ^- beam momentum and azimuthal angle distributions for the $\theta_h = +3$ and -3 samples. Note that the differences between the two sets of data arising from differing targeting conditions are well produced by the Monte Carlo simulation. In Fig. 10 angular distributions (dip) in the y-z plane for $\theta_V = +3$ and -3 data are shown. The shapes of these distributions are clearly quite different. This is due to the transverse momentum dependence of the Σ^- production process. In the case of the $\theta_V = -3$ data, protons were directed downward toward the target, and thus more Σ^- hyperons were produced going downward; the opposite was true for $\theta_v = +3$ data.

Figure 11 shows the electron c.m. angular distribution projected onto the x and z axes. Since these are distributions for θ_h data, there is no Σ^- polarization in the x and z directions. As expected, the z distribution shows that backward electrons are not detected by our apparatus. The concave shape of the x distributions is simply a kinematic reflection of this loss.

Effective-mass distributions for two-body decays and beta decays are shown in Fig. 12. The long high-mass tail in Fig. 12(b) is primarily due to multiple Coulomb scattering of the Σ^- beam in the PWC region. The generally good agreement between our Monte Carlo results and the experimental data indicates that we have appropriately modeled our apparatus.

V. LEPTONIC DECAY IDENTIFICATION AND DATA REDUCTION

A. Electron-hadron discrimination

The principal background in this experiment is the dominant decay mode $\Sigma^- \rightarrow n\pi^-$. Two detectors (TRD and LGC) were used to discriminate between e^- and π^-. The beta-decay event trigger involved only the TRD.

Because most of the π^-'s accepted by the trigger were events that showered in the TRD (the TRD is $\approx 6\%$ of an absorption length), a careful study of the TRD was performed using 30-GeV/c e^- and π^- beam runs.

Table III shows the standard electron-identification cuts used in the analysis. These involved selections on the charged-particle multiplicity as seen by the multiplicity counters behind the lead-glass array (LGS5) and following the TRD (MC). They also involved cuts on the total number of clusters detected by the TRD, the ratio of the energy measured by the LGC to the momentum measured in the charged-particle spectrometer, and cuts on the electromagnetic shower profile in the LGC. We define w_i to be the fractional energy deposited in layer i of the LGC. We then compute Δw_i, the difference between the measured value and the theoretical average value for electrons as calculated using Rossi's[46] approximation A. Table III displays the numerical values of the cuts. The adequacy of Rossi's formula for this calculation was checked using our 30-GeV/c e^- beam data. The agreement was quite good (see also Ref. 43).

These e^- cuts were studied using our e^- beam runs at nominal momenta of 10, 20, 30, 40, and 50 GeV/c. The e^- inefficiency is 3% and shows no momentum bias (Fig. 13).

Our nonleptonic background was estimated to be $(2.3\pm0.3)\%$ and $(1.8\pm0.3)\%$ for θ_v and θ_h data, respectively (Fig. 14). Moreover, by reconstructing the effective mass of the event sample on either side of the E/P peak, we were able to identify its components. The process $\Sigma^- \rightarrow n\pi^-$ accounts for 0.6% (θ_h) and 1% (θ_v). The decay $\Xi^- \rightarrow \Lambda\pi^-$ contributes 0.9% (θ_h) and 1% (θ_v).

Even though we had 3.4 radiation lengths of lead in front of the LGC to start electromagnetic showers early, the cracks between lead-glass blocks (Figs. 4 and 13) still influenced some shower profiles. In the vicinity of the cracks, e^- inefficiency was higher due to the shower profile cut. These crack effects were studied using runs in which the LGC moved across a stationary 30-GeV/c e^- beam. Softer LGC cuts were devised to minimize the crack effect and are also shown in Table III. The hadronic background is 5.7% and e^- inefficiency 1.5% for this softer version of the e^- identification cuts. At the cracks, the maximum inefficiency is 3% compared to 8% for the harder (standard) cuts discussed above. Both versions were used to analyze our final data sample. The systematic error associated with LGC cracks was then estimated using the difference of the results.

B. Data reduction

Events from the beta-decay trigger were analyzed by the PWC and DC tracking programs. Using the Monte Carlo simulation, we verified that the losses in PWC tracking were consistent with expectations from Σ^- decays in the PWC region. Our DC single-track efficiency

TABLE III. Electron-identification cuts used in the analysis. See text for definition of symbols and abbreviations. MIP's denotes minimum-ionizing particles.

	Standard electron cuts	Soft electron cuts
MC	<6 MIP's	Same
TRD	<8 clusters if MC <2 MIP's <9 clusters otherwise	Same
LGS5	<3 MIP's	Same
E/P	$0.92 < E/P < 1.12$	$0.85 < E/P < 1.20$
Δw_1	$-0.20 < \Delta w_1 < 0.36$	$\Delta w_1 < 0.50$
Δw_2	$-0.28 < \Delta w_2 < 0.20$	$\Delta w_2 < 0.22$
Δw_3	$-0.10 < -\Delta w_3 < 0.17$	$-\Delta w_3 < 0.30$
Δw_4	$-0.10 < -\Delta w_4 < 0.07$	$-\Delta w_4 < 0.14$

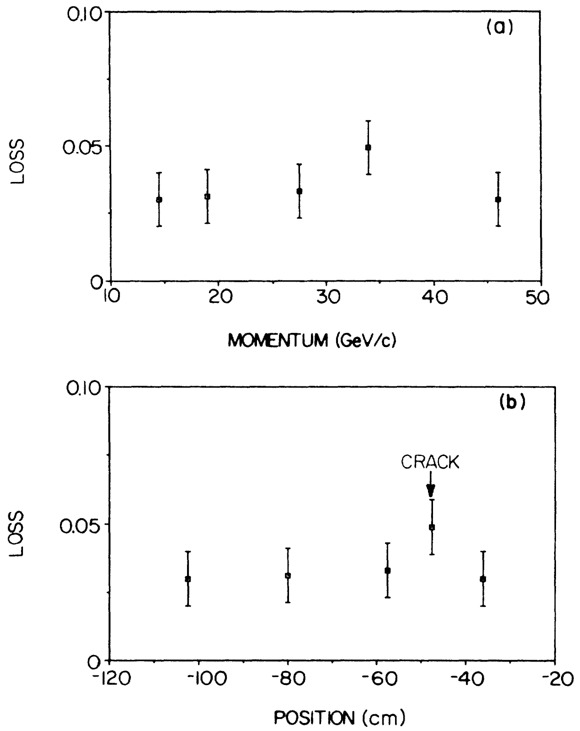

FIG. 13. Electron cut inefficiencies. In (a) the losses are plotted as a function of electron momentum. The same data are plotted in (b) with the horizontal axis now the position where the electron beam hits the LGC. The position of a crack between the lead-glass blocks is shown by an arrow. This crack is responsible for the higher loss near 34 GeV/c in (a).

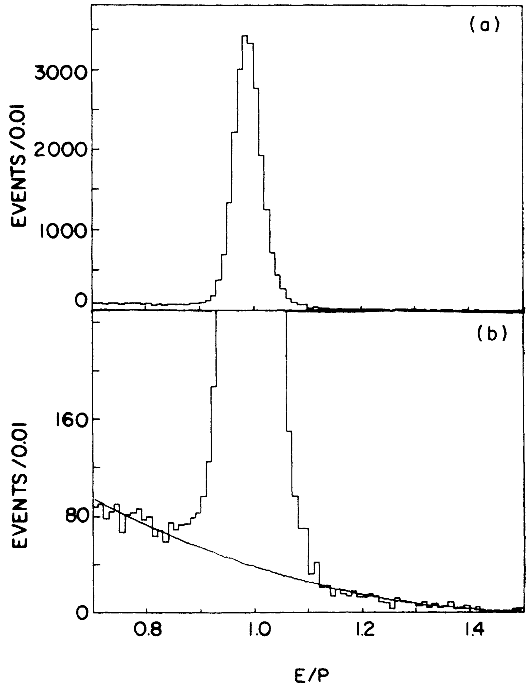

FIG. 14. (a) E/p distribution for $\Sigma^- \to n e^- \bar{\nu}$ electron candidates showing the background level. The vertical scale is expanded in (b) to show the background extrapolation under the E/p peak.

was 98%. We rejected multitrack events.

The e^- identification cuts were then imposed on events that passed the tracking program successfully. Some geometrical and kinematic cuts were also imposed on the data. Events were rejected if any of the following criteria were not satisfied.

(1) 220 GeV/c $<\Sigma^-$ momentum <275 GeV/c.

(2) 2 m $<z$ position of the decay vertex <18 m.

(3) Extrapolation of the Σ^- to the target agrees with the vertical proton beam position within ± 2.5 mm.

(4) 12.5 GeV/c $<e^-$ momentum <50 GeV/c to ensure an LGC acceptance greater than 90%.

(5) More than 1% of the total NC shower energy deposited after the first 14 counters. (This cut eliminated all electromagnetic shower events in the NC, particularly those from $K^- \to e^- \pi^0 \bar{\nu}$ decays.)

(6) 124 GeV $<$ NC energy <297 GeV.

(7) Neutron-calorimeter fiducial-volume cut. (Events reconstructed within 4 cm of the edges of the NCPWC's were discarded.)

VI. ASYMMETRIES

A. Bias-canceling method

Experimentally, the *observed* c.m. angular distribution can be represented by multiplying the right-hand side of Eq. (2.5) by $A(p,\omega,z,\mathbf{p}_{\Sigma^-})$ where A is the experimental acceptance. The acceptance is a function of the pertinent decay product c.m. momentum p, the unit vector ω in the direction of p, the decay vertex z position, and the Σ^- momentum vector $\mathbf{p}_{\Sigma^-}$. This function does not change if only the polarization is reversed. Experimentally, the polarization was reversed by reversing the targeting angle. This not only changed the polarization but also changed the Σ^--beam phase-space distribution due to the p_t dependence of the production process and, in the case of θ_h data, slightly different proton beam positions. Thus, after integrating over z and $\mathbf{p}_{\Sigma^-}$, the acceptance was somewhat different for different targeting angles.

To remove this target-angle-dependent bias, the data were weighted according to the beam phase-space variable which was most sensitive to the decay product acceptance. The variable chosen for the θ_h data was the azimuthal angle (ϕ) of the Σ^- particle. For the θ_v data the relevant parameter was the dip angle (λ). Weighting effectively selected the events in the overlapping region of the ϕ or λ distributions. The effect of the weighting on Σ^- beam distributions can be seen in Fig. 15. It reduced the statistics by half. We used Monte Carlo events to verify that the weighting procedure did not change the asymmetry parameters. We also analyzed the data without weighting. The results were consistent with those obtained with weighting.

After integration over z and $\mathbf{p}_{\Sigma^-}$, the acceptance is a function of p and ω. If we integrate over p also, the formula is reduced to a function of ω only.

We then have

$$\frac{dN}{d\Omega}=\frac{N}{4\pi}A(\omega)(1+\alpha\mathbf{P}\cdot\omega)\ , \tag{6.1}$$

where $A(\omega)$ is the acceptance, α is the asymmetry parameter averaged over the acceptance, ω is the unit vector in the direction of solid-angle element $d\Omega$, and $\mathbf{P}$ is the polarization vector. Note that α in Eq. (6.1) may be different from the true theoretical value. Because of our large experimental acceptance, the α_e and α_n do not require correction. The correction applied to α_ν was also small.

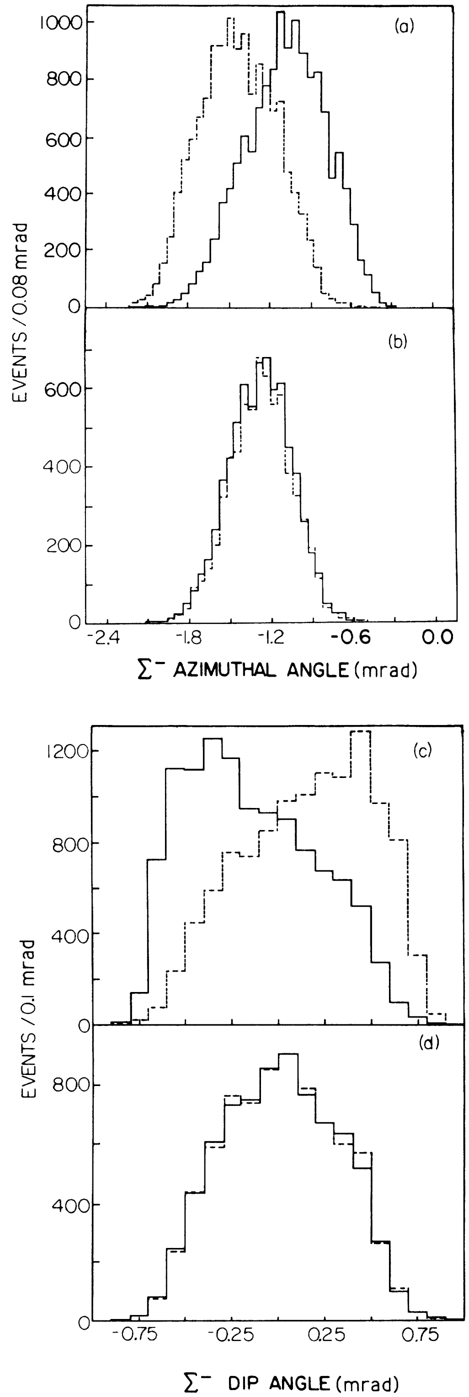

FIG. 15. The effects of weighting are shown by comparing pairs of the above figures. (a) and (b) show the horizontal angular distribution in the x-z plane (azimuth) before and after weighting for $\theta_h = -3$ (solid line) and $+3$ mrad (dashed line). The pair (c) and (d) compare the distributions in the y-z plane (dip).

We write the components of polarization:

$$P_x = P\sin\Psi\cos\xi,\quad P_y = P\cos\Psi,\quad P_z = P\sin\Psi\sin\xi\ .$$

Here Ψ is the polar angle relative to the y axis and ξ is the azimuthal angle in the x-z plane, all in the c.m. frame. In the case of θ_v data, Ψ is 90° and ξ is the spin-precession angle. They are both zero for θ_h data.

A total of 90 bins (9 in the cosine of the polar angle and 10 in azimuthal angle) was used for the c.m. decay-angular distribution for each targeting angle. Data for all targeting angles were fit simultaneously to Eq. (6.1) by a maximum-likelihood method with 95 parameters. Of these, 90 gave the acceptance in each bin, two for relative normalizations, the rest were Ψ, ξ, and αP.

B. The measured asymmetries

Table IV lists the fitted values of αP, ξ, and Ψ, derived from the above procedure for the horizontal and vertical targeting data for both the pion ($\Sigma^- \to n\pi^-$) and electron ($\Sigma^- \to ne^-\bar{\nu}$) final states. To display the projections of the angular distribution, we define F_{+i} (F_{-i}) to be the fraction of events in the ith $\cos(\theta)$ bin for positive (negative) targeting angle, where θ is the polar angle between the decay particle momentum and the Σ^- polarization vector. Then the ratio $[(F_{-i}-F_{+i})/(F_{-i}+F_{+i})] = \alpha P\cos(\theta_i)$. These ratios are plotted in Figs. 16–18. For the $\Sigma^- \to n\pi^-$ decay the asymmetry is known[18] to be $\alpha_\pi = +0.068 \pm 0.008$. From a sample of 1.04×10^6 of these decays we measured $\alpha_\pi P$ (Table IV) and thereby determined the polarization of the Σ^- beam.

The larger precession angles (ξ) observed for the neutron and antineutrino in Table IV (θ_v data) are a result of neutron-calorimeter resolution effects. The x (y) asymmetries were determined by comparing the number of decay particles which decayed right (up) with those that decayed left (down). This measurement was simplified because the sense of left or right (up or down) was very

TABLE IV. Results of uncorrected fits to the angular distributions for both θ_h and θ_v data. ξ is the Σ^- precession angle which is constrained to be zero for the θ_h data. Ψ is the polarization angle relative to the y axis; it is expected to be zero for θ_h data and 90° for θ_v data. All angles are in degrees, and the errors are statistical only.

		αP	ξ (deg)	Ψ (deg)
θ_h	e^-	-0.117 ± 0.014	0	1 ± 7
	n	0.131 ± 0.015	0	1 ± 7
	$\bar{\nu}$	-0.057 ± 0.016	0	15 ± 16
	π^-	0.0154 ± 0.0026	0	1 ± 10
θ_v	e^-	-0.128 ± 0.019	129 ± 8	81 ± 6
	n	0.084 ± 0.015	159 ± 11	85 ± 10
	$\bar{\nu}$	-0.032 ± 0.016	200 ± 29	101 ± 30
	π^-	0.0177 ± 0.0042	125 ± 14	79 ± 14

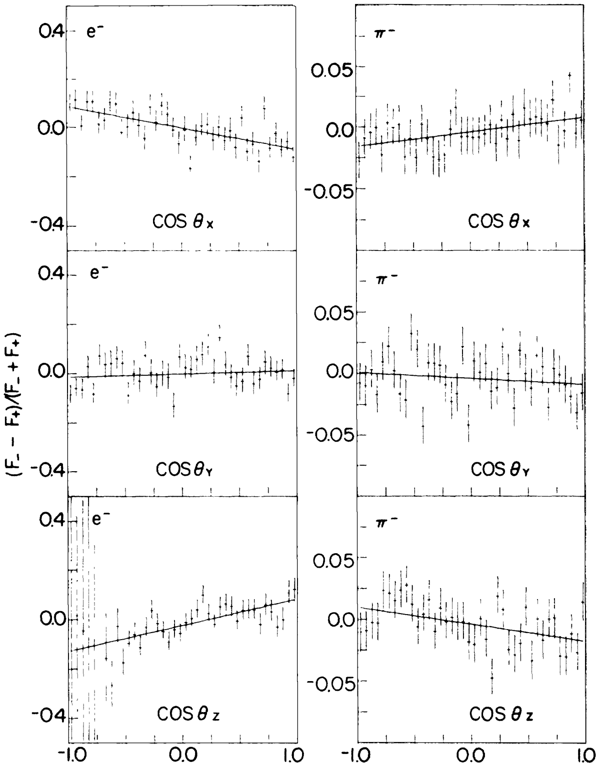

FIG. 16. Electron and pion c.m. decay distributions for θ_v data. Parity conservation in the Σ^- production process requires a zero slope for the cos(θ_y) distributions. Note the differing ordinate scales for the pion and electron plots.

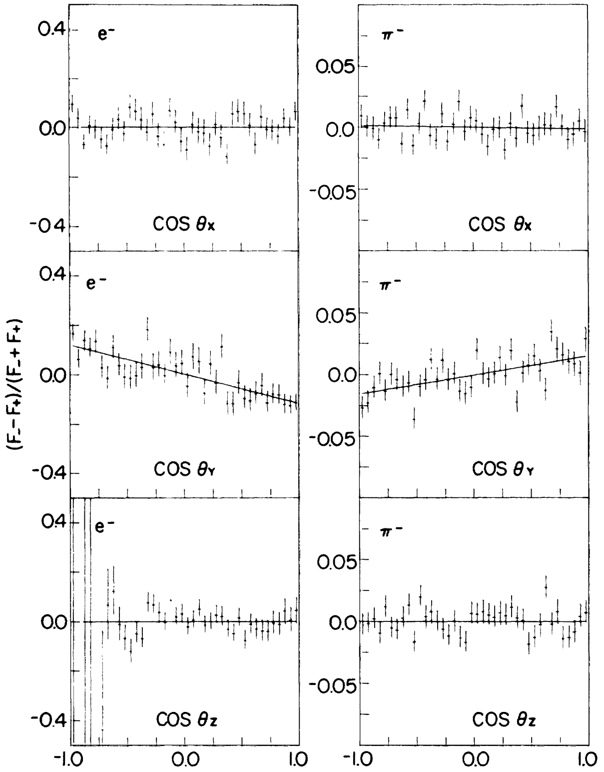

FIG. 17. Electron and pion c.m. decay distributions for θ_h data. Parity conservation in the Σ^- production process requires zero slope for the cos(θ_x) and cos(θ_z) distributions. Note the differing ordinate scales for the pion and electron plots.

nearly the same in the c.m. frame as it was in the laboratory. However, the z asymmetries depend on an accurate neutron momentum reconstruction to determine the center-of-mass polar angle. The neutron and antineutrino (but *not* the electron) z asymmetries thus depend on the neutron-calorimeter resolution which was studied extensively using calibration data and Monte Carlo simulations. This led us to apply a small correction which increased the measured neutron and antineutrino z asymmetries by 0.037±0.002 and 0.020±0.002, respectively. The q^2 dependence of α_ν (see Fig. 20 below) combined with our finite acceptance gave rise to an additional correction of 0.004 (0.001) to the y (x) component of the antineutrino asymmetry for the θ_h (θ_v) data.

We also did the fit assuming the polarizations were different from +3 and −3 mrad targeting angle. The results were consistent statistically. The measured asymmetries were also corrected for background due to the decays $\Sigma^- \rightarrow n\pi^-$ and $\Xi^- \rightarrow \Lambda\pi^-$ (1.5±0.3% for θ_h and 2.0±0.3% for θ_v) assuming a uniform center-of-mass angular distribution. The corrected results are presented in Table V. The errors quoted for αP include an allowance for possible electron background from the reactions $\Xi^- \rightarrow \Lambda e^- \bar{\nu}$ (1%) and $\Sigma^- \rightarrow \Lambda e^- \bar{\nu}$ (1%) as well as the uncertainty in the hadronic background estimate. We note that the values of ξ in Table V are statistically compatible. Reference 23 describes the determination of the Σ^- magnetic moment from the electron and pion precession angles.

Since the horizontal and vertical targeting angles are the same (see Table II), we use a common polarization. This assumption is confirmed by the fact that the hor-

TABLE V. Data from Table IV after resolution, acceptance, and background corrections (described in text) were applied. Both statistical and systematic errors are shown.

	αP for θ_h	αP for θ_v	ξ (deg) for θ_v
e^-	−0.119 ±0.014±0.003	−0.130 ±0.019±0.003	129±8
n	0.132 ±0.015±0.003	0.105 ±0.015±0.003	139±11
$\bar{\nu}$	−0.062 ±0.016±0.002	−0.044 ±0.016±0.001	134±29
π^-	0.0154±0.0026±0.0010	0.0177±0.0042±0.0021	125±14

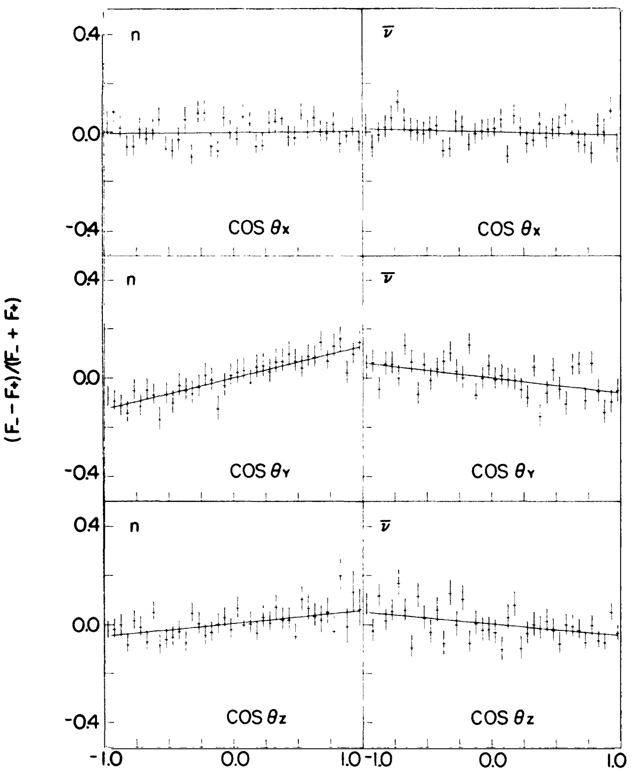

FIG. 18. Neutron and antineutrino c.m. decay distributions for θ_h data. Parity conservation in the Σ^- production process requires zero slope for the $\cos(\theta_x)$ and $\cos(\theta_z)$ distributions.

izontal and vertical asymmetries are statistically compatible. Thus we combine the vertical and horizontal targeting asymmetries with the known[18] value of α_π to obtain

$$P=+0.236\pm0.043,\quad \alpha_e=-0.519\pm0.104\ ,$$

$$\alpha_n=+0.509\pm0.102,\quad \alpha_\nu=-0.230\pm0.061\ ,$$

where the stated errors include an 11.8% scale uncertainty due to the uncertainty in α_π. These values supersede earlier published[16] results from a subsample of the data.

C. Determination of the sign of g_1/f_1

One of our primary reasons for performing this experiment was to resolve the controversy[3,5–9] regarding the sign of g_1/f_1 for $\Sigma^-\rightarrow ne^-\bar{\nu}$ decay. To ensure an unambiguous result, we have developed three distinct methods for the sign determination. Two of these are *independent* of the sign of the $\Sigma^-\rightarrow n\pi^-$ asymmetry parameter α_π.

The first method involves a direct comparison of two-body data and beta-decay data. Figures 16 and 17 display c.m. angular distributions for electrons (pions) from the decay $\Sigma^-\rightarrow ne^-\bar{\nu}$ ($\Sigma^-\rightarrow n\pi^-$). Examination of these shows that the slopes of the electron and pion distributions are opposite in sign. Since the slopes are just projections of αP, α_e and α_π must have opposite signs. The measured[18] value $\alpha_\pi=+0.068\pm0.008$ then requires α_e to be negative (independent of any particular definition of coordinate systems, etc.). Finally, as shown in Fig. 19, our negative value for α_e implies a negative value for g_1/f_1. Similar arguments for α_n and α_ν yield the same conclusion. Thus, *given the published sign for* α_π, the sign of g_1/f_1 is definitively established.

We can also use the "self-analyzing" character[47] of hyperon beta decays to determine the sign of g_1/f_1. To do this we consider both possibilities for the sign of α_π. If it is positive, the beta-decay asymmetries are as given in the previous section; if it is negative, then α_e, α_n, and α_ν have their signs reversed. Performing χ^2 fits to both sets of values (with $|g_1/f_1|=0.327\pm0.020$ as discussed later in Sec. VII B) then shows that a negative g_1/f_1 (and the corresponding positive α_π) is favored by more than 5 standard deviations.

Finally, with a large data sample, the sign of g_1/f_1 can be determined by exploiting the q^2 dependence of α_e and α_ν. Since q^2 is the mass squared of the electron and antineutrino system, their momentum vectors (in the Σ^- rest frame) point in the same direction at $q^2=0$ and oppositely at the maximum q^2. Therefore α_e and α_ν have the same signs at $q^2=0$ and opposite signs at maximum q^2. Between these limits either α_e or α_ν must change sign depending on the value of g_1/f_1. Obviously this signature is independent of the sign of α_π. In Fig. 20 we plot $\alpha(q^2)P$ as a function of q^2. The solid curve is the expected dependence assuming $g_1/f_1=-0.327$ (corresponding to positive P and α_π). The dashed curve shows the behavior if $g_1/f_1=+0.327$ (P and α_π negative). Clearly,

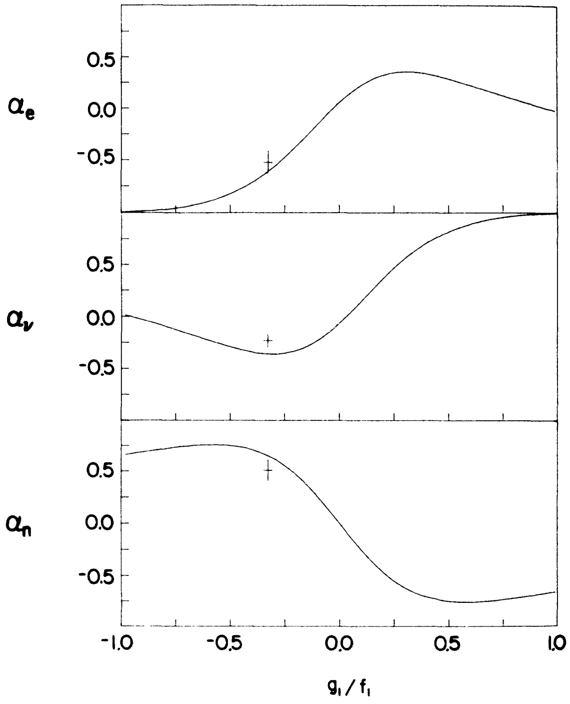

FIG. 19. The asymmetry parameters α_e, α_n, and α_ν plotted as a function of g_1/f_1. We also plot our experimental values of these parameters at $g_1/f_1=-0.327\pm0.20$. We have set $f_2/f_1=0.96$ and $g_2=0$ for these calculations.

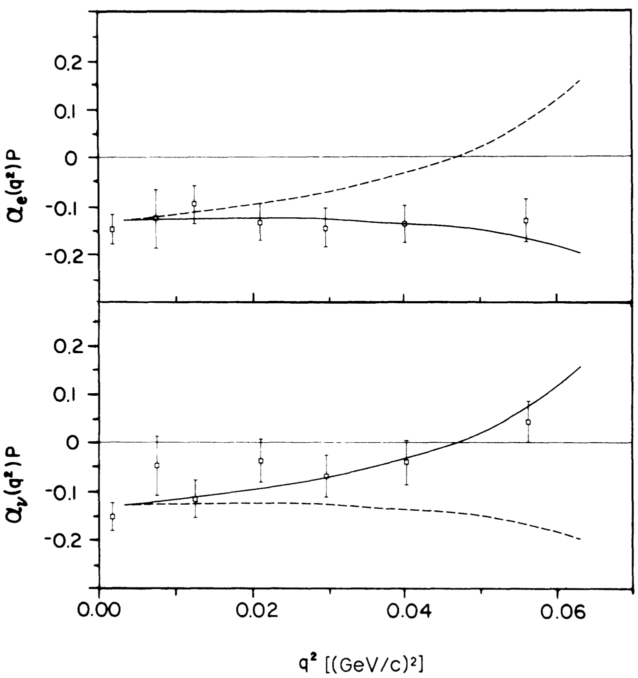

FIG. 20. The q^2 dependence of the asymmetries $\alpha_\nu P$ and $\alpha_e P$. The solid curves are the calculated q^2 dependences assuming $g_1/f_1=-0.327$ and positive α_π and P. The dashed curves assume $g_1/f_1=+0.327$ and negative α_π and P. Since only the solid curve fits the data, we conclude that g_1/f_1 is negative.

the data are *only* consistent with negative g_1/f_1 and positive P and α_π.

These three methods conclusively establish that the sign of g_1/f_1 is negative. They also substantiate the published sign for α_π and the Σ^- polarization P.

D. A check of time-reversal invariance

A correlation between the plane of the decay leptons and the Σ^- polarization vector in $\Sigma^- \rightarrow n e^- \bar{\nu}$ would indicate a violation of time-reversal symmetry. We have therefore looked for a term of the form[48] $\alpha_T \mathbf{P}\cdot\hat{\mathbf{p}}_e \times \hat{\mathbf{p}}_\nu$ in the decay-angular distribution. Applying the same bias-canceling techniques we used to determine the parity-violating α's, we obtain the result $\alpha_T=0.11\pm0.10$, consistent with time-reversal invariance.

VII. FITS TO THE NEUTRON AND ELECTRON SPECTRA

A. Form-factor determination

This experiment has at least an order of magnitude more events than any previous experiment. Its considerably higher statistical power means that effects neglected in previous experiments must now be carefully considered.

It has been pointed out in a previous experiment[15] that g_1 and g_2 are highly correlated. Specifically, measurements of the neutron spectrum or the e-$\bar{\nu}$ correlation probe only the correlation $g_1-0.237g_2$. Previous hyperon beam measurements of the axial-vector form factor with unpolarized Σ^- are of this kind, so it has been necessary to assume $g_2=0$ in order to obtain a value for g_1/f_1. The present measurements of asymmetries with respect to the Σ^- polarization in addition to the Dalitz plot provide, for the first time, some sensitivity to g_1 and

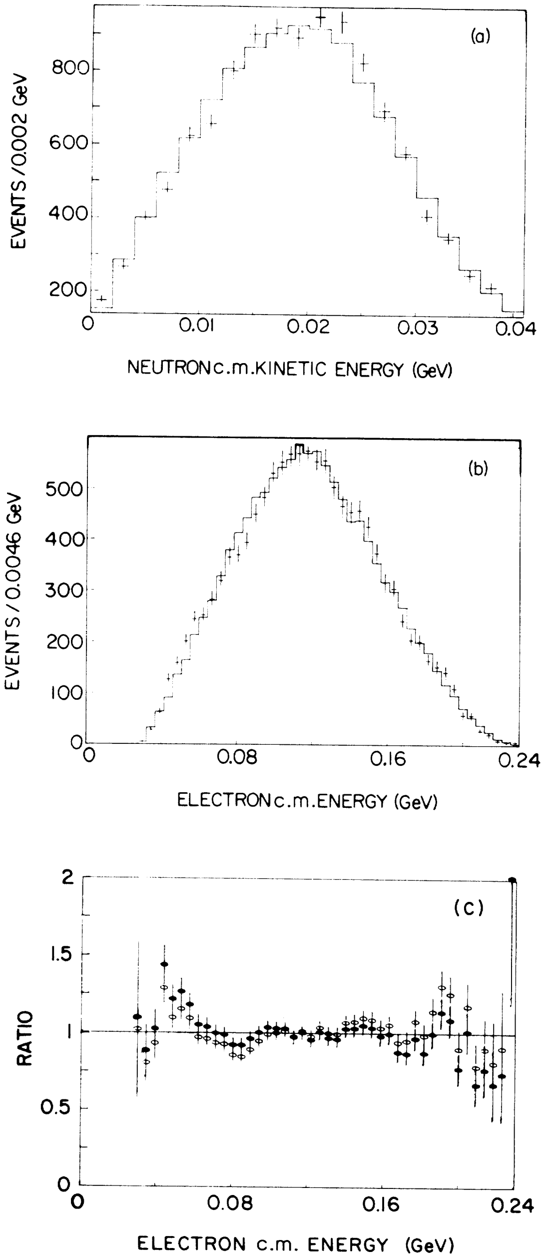

FIG. 21. The $\theta_h=-3$ mrad data sample. (a) The neutron c.m. kinetic energy (T) distribution. The solid line is the Monte Carlo fit to the data with $|g_1/f_1|=0.340$. (b) The electron c.m. energy (E_e) spectrum. The solid line represents the best fit to the data yielding $f_2/f_1=-0.90\pm0.15$. (c) The sensitivity of the data to f_2 is demonstrated by showing the ratio of the data to the Monte Carlo fit. The solid circles correspond to the best fit. The open circles correspond to $f_2=0$.

TABLE VI. A summary of $|g_1(0)/f_1(0)|$ and $f_2(0)/f_1(0)$ values as determined from the separate data samples assuming $g_2=0$, together with values of χ^2/number of degrees of freedom (χ^2/N_{DF}).

		$\lvert g_1(0)/f_1(0)\rvert$	χ^2/N_{DF}	$f_2(0)/f_1(0)$	χ^2/N_{DF}
θ_h	+3	0.340±0.015	1.07	−1.10±0.15	1.65
	0	0.325±0.025	1.19	−1.35±0.25	1.36
	−3	0.340±0.015	1.89	−0.90±0.15	1.77
θ_v	+3	0.300±0.015	1.14	−0.80±0.15	0.87
	0	0.310±0.020	1.05	−1.40±0.25	1.41
	−3	0.340±0.015	1.92	−0.75±0.15	0.96
Combined		0.327±0.007		−0.96±0.07	

g_2 separately. In the following we will first present our results making the conventional assumption of $g_2=0$. Subsequently we will use our asymmetry results as well as information from the Dalitz-plot variables to investigate the possible range of values of g_2/f_1.

For the two Dalitz-plot c.m. variables we choose the electron energy E_e and the neutron kinetic energy T. We note (see Appendix A) that, to a very good approximation, the neutron spectrum depends only on $|g_1/f_1|$ if we assume g_2 is zero. This yields a determination of $|g_1/f_1|$ independent of the electron spectrum and its inherent sensitivity to radiative corrections. Experimentally, the electron-antineutrino correlation is poorly determined because extra photons produced by electron bremsstrahlung or internal radiation render the calculation of the energy and momentum of the antineutrino uncertain. Although we choose to use the neutron spectrum to determine $|g_1/f_1|$, we note that a full Dalitz-plot analysis for $|g_1/f_1|$ also yields consistent results.

The main contribution of f_2 to the differential decay rate is proportional to the product E_eT. Thus, its largest contribution to the Dalitz plot is along the diagonal. Using the neutron spectrum to fix $|g_1/f_1|$, we then use this value and the electron spectrum to determine f_2/f_1. Finally, using the electron and neutron spectra combined with the measured asymmetries, we investigate g_2/f_1.

B. Determination of $|g_1/f_1|$

The magnitude of g_1/f_1 has been measured by many experiments[11-15] using a variety of techniques which include fitting to the neutron energy, the full Dalitz plot, or the electron-antineutrino correlation. We determine T independent of the electron kinematics from the measured Σ^- and neutron energy-momentum four-vectors:

$$(P_\Sigma-P_n)^2=M_\Sigma^2+M_N^2-2M_\Sigma M_n-2M_\Sigma T\ .$$

Figure 21(a) displays the neutron spectrum for the $\theta_h=-3$ mrad data. A fit to this data with $g_2=0$ and $f_2/f_1=-0.96$ yields $|g_1/f_1|=0.340$ at $q^2=0$. (The q^2 dependence of f_1 and g_1 has been included in the analysis.) In Table VI we give the results for each of the data sets. The weighted mean and its statistical uncertainty are $|g_1(0)/f_1(0)|=0.327\pm0.007$.

The systematic uncertainties in $|g_1/f_1|$ come from a variety of sources identified in Table VII. We use a sample of $\Sigma^-\rightarrow n\pi^-$ events (taken simultaneously with the leptonic data) to provide kinematically constrained neutrons for the calibration of our neutron calorimeter. The neutron resolution function has a non-Gaussian tail (see Fig. 7) contributed by neutrons which interacted upstream of the calorimeter. Our calibration has a slight sensitivity to the cuts used to remove this tail. By requiring agreement between the measured and predicted neutron energy, the sensitivity of $|g_1/f_1|$ to this cut was reduced to 0.008.

Since $|g_1/f_1|$ is only weakly sensitive to f_2/f_1, a variation of f_2/f_1 from −0.10 to −1.10 causes $|g_1/f_1|$ to change by only 0.010. Other systematic effects were checked by varying the geometrical and kinematical cuts. Background subtraction was done by considering events with electron candidates in the regions (see Fig. 14) $0.82<E/P<0.92$ and $1.12<E/P<1.22$ as background and estimating the contribution of these events to the final sample. This background subtraction increased $|g_1/f_1|$ by less than 0.010.

Both hard- and soft-electron identification cuts were used to check the sensitivity to electron losses. We also estimated our sensitivity to the q^2 dependence of f_1 and g_1: if we assume no q^2 dependence, $|g_1/f_1|$ increases by 0.045. The error due to the uncertainty in q^2 dependence was taken to be 0.016. This was calculated assuming that the Σ^- form-factor pole masses can vary from the values we assumed to those of nucleon form-factor pole masses. Combining all of these systematic errors (Table VII) with the statistical error gives $|g_1(0)/f_1(0)|=0.327\pm0.020$. A comparison with previous experiments is shown in Table VIII.

TABLE VII. Summary of the sources and magnitudes of uncertainties in the determination of $|g_1(0)/f_1(0)|$.

Uncertainty source	Magnitude
Uncertainty from q^2 dependence	0.016
Neutron calorimeter calibration	0.008
Uncertainty in f_2	0.005
Uncertainty from background subtraction and lead-glass-calorimeter cracks	0.005
Momentum calibration	<0.001
Neutron-counter resolution used in Monte Carlo simulation	<0.001
Combined systematic uncertainty	0.019
Statistical uncertainty	0.007
$\lvert g_1(0)/f_1(0)\rvert=0.327\pm0.020$	

TABLE VIII. Comparison of neutron spectrum results for $|g_1/f_1|$ with other experiments. Results are shown for both constant f_1 and g_1 and with q^2 dependence. The values of M_A and M_V given in Sec. II and the procedure discussed in Ref. 9 were used to correct results given in Refs. 10–14 for the q^2 dependence of f_1 and g_1.

Reference	Events	$\lvert g_1/f_1\rvert$ ($f_1,g_1=\text{const}$)	$\lvert g_1/f_1\rvert$ ($f_1,g_1 q^2$ dep)
Colleraine *et al.* (Ref. 11)	49	0.23 ± 0.16	0.17 ± 0.17
Eisele *et al.* (Ref. 12)	33	$0.36^{+0.26}_{-0.19}$	$0.31^{+0.26}_{-0.22}$
Baltay *et al.* (Ref. 13)	36	0.29 ± 0.28	$0.24^{+0.28}_{-0.24}$
Tanenbaum *et al.* (Ref. 14)	3 507	0.435 ± 0.035	0.385 ± 0.037
Decamp *et al.* (Ref. 10)	519	$0.17^{+0.07}_{-0.09}$	$0.09^{+0.07}_{-0.09}$
Bourquin *et al.* (Ref. 15)	4 456	0.40 ± 0.05	0.35 ± 0.05
This experiment	49 671	0.372 ± 0.020	0.327 ± 0.020

C. Determination of f_2/f_1

We exploit the sensitivity of the electron energy spectrum to f_2/f_1. Fixing $g_1/f_1=-0.327$ and $g_2=0$, we fit the E_e spectrum to determine f_2/f_1. As above, we include the q^2 dependence of the form factors in the fit. Figure 21(b) shows the measured electron spectrum for the $\theta_h=-3$ mrad data sample along with the Monte Carlo fit to the data. Table VI gives the results from all of the data samples. When combined, they give $f_2(0)/f_1(0)=-0.96\pm0.07$, where the error is statistical only.

External bremsstrahlung and radiative corrections are significant when fitting the E_e spectrum and are included in the above analysis. The magnitude of f_2/f_1 would decrease by 0.10 if no radiative corrections were applied. We have applied radiative corrections as calculated by Töth, Margaritisz, and Szegö[36,37] to our data. If instead we used the calculation of Garcia and Kielanowski[17] (which is less directly applicable to this experiment), f_2/f_1 would change by 0.05. We take half of this difference as the residual systematic uncertainty due to the radiative corrections.

The material between the average hyperon decay vertex and the first spectrometer magnet (Fig. 1) represents $(5.94\pm0.20)\%$ r.l. which gives rise to an uncertainty of 0.02 in f_2/f_1.

The θ_v data have one additional source of uncertainty. The electron acceptance of our apparatus is sensitive to the z component of the hyperon polarization since forward and backward electrons (in the c.m.) have very different laboratory acceptances. Because the θ_v data have such a z component of polarization, f_2/f_1 values obtained from them have an additional uncertainty of 0.10.

Our largest systematic error arises from the uncertainty in the momentum calibration of the hyperon and spectrometer magnets. This contributes an uncertainty of 0.10 in f_2/f_1. Varying g_1/f_1 within its total error changes f_2/f_1 by less than 0.05. Other systematic checks were performed by varying our geometrical and kinematic cuts. Both hard- and soft-electron identification cuts were used to check the sensitivity to the lead-glass "cracks." We estimate that this contributes an uncertainty of 0.04. Ignoring the q^2 dependence of f_1 and g_1 would increase the magnitude of f_2/f_1 by 0.05.

After combining all of these uncertainties (summarized in Table IX), we find a total systematic error in f_2/f_1 of 0.13, giving a final value of $f_2(0)/f_1(0)=-0.96\pm0.15$ (including both statistical and systematic uncertainties).

D. Investigation of g_2/f_1

In Sec. VII A we stressed the fact that g_1 and g_2 are correlated in any Dalitz-plot analysis, and in Sec. VII B we determined $|g_1/f_1|$ under the assumption that $g_2=0$. We now relax this assumption and use the neu-

TABLE IX. Summary of the sources and magnitudes of the uncertainties in the determination of $f_2(0)/f_1(0)$.

Uncertainty source	Magnitude
Momentum calibration	0.10
z-polarization uncertainty (θ_v data only)	0.10
Uncertainty from radiative corrections	0.03
LGC cracks	0.04
Uncertainty from radiating material in beam	0.02
Uncertainty in q^2 dependence	0.02
Combined systematic uncertainty	0.13
Statistical uncertainty	0.07
$f_2(0)/f_1(0)=-0.96\pm0.15$	

TABLE X. A summary of the fits to the asymmetry parameters and the g_1, g_2 correlation from the neutron spectrum. See text for description of fits.

Fit	$g_1(0)/f_1(0)$	$g_2(0)/f_1(0)$	P	α_π	$\chi^2/N_{\rm DF}$
1	-0.20 ± 0.08	0.56 ± 0.37	0.240 ± 0.040	0.068 ± 0.008	1.07/2
2	-0.21 ± 0.09	0.49 ± 0.40	0.231 ± 0.040	0.068 ± 0.008	0.65/1
3	-0.18 ± 0.09	0.92 ± 0.49	0.235 ± 0.040	0.068 ± 0.008	0.02/1
4	-0.328 ± 0.019	0 (fixed)	0.192 ± 0.014	0.073 ± 0.006	2.52/3

tron energy spectrum to determine g_1/f_1 as a function of g_2/f_1. This yields the relation $g_1/f_1-0.237g_2/f_1=-0.327\pm0.020$ in good agreement with Ref. 15.

To extract g_2/f_1, we combine the asymmetry parameters (α_e, α_n, α_ν) with this relation to make a general fit. We also include in this fit the significant uncertainty in $\alpha_\pi P$ and in α_π. Specifically, the quantities used as input to the fit are $(\alpha_e+\alpha_n)P$, $(\alpha_\nu+\alpha_n)P$, $(\alpha_e+\alpha_\nu)P$, $\alpha_\pi P$, α_π, and the constraint $g_1/f_1-0.237g_2/f_1=-0.327\pm0.020$. We use the sums of the asymmetries rather than the asymmetries themselves because, to a good approximation, they are statistically independent (see Appendix B). The polarizations of the horizontal and vertical targeting data are taken to be the same, and f_2/f_1 is fixed at -0.96. The results are given as fit 1 in Table X. An additional error of 0.002 has been assigned to g_1/f_1 due to the uncertainty in f_2/f_1. In Fig. 22 we plot the χ^2 contour for g_1/f_1 vs g_2/f_1. The two contours represent 1σ and 2σ. We note that the result for g_2/f_1 is only 1.5σ from zero, and that negative values of g_2/f_1 are clearly disfavored.

It can be argued that, since the antineutrino momentum vector was not directly measured, it could have unexpected biases which might favor a nonzero value of g_2/f_1. We point out that, for the θ_ν data, our antineutrino precession angle is consistent with the precession angle of the electron, neutron, and pion (Table V). However, we have repeated the fit excluding the antineutrino asymmetry measurement. This is listed as fit 2 of Table X. Although it gives a somewhat lower value of g_2/f_1, this fit is clearly consistent with fit 1.

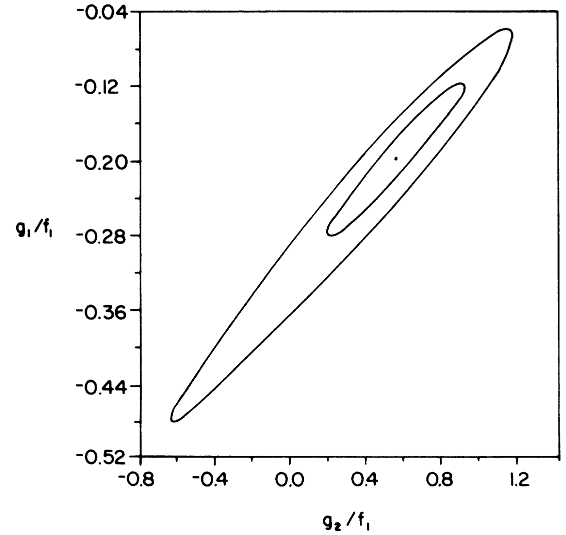

FIG. 22. χ^2 contours for the overall fit to the data for both g_1/f_1 and g_2/f_1. The two curves represent 1σ and 2σ intervals, and the dot is our best fit.

It is also of interest to do the fit with the g_1, g_2 correlation constraint removed, using only the asymmetry parameters. The results are shown in Table X as fit 3. As expected, the nonzero value of g_2 comes mainly from the interplay of the three asymmetry parameters.

Since they arise from the asymmetry parameters, the values of g_2/f_1 in Table X are sensitive to our knowledge of P and therefore also of α_π. A small polarization with a correspondingly larger α_π could accommodate the asymmetries to $g_2=0$, as shown by fit 4 in Table X. This has been explored in greater detail by Razis[49] with a subsample of the data.

Since the Σ^- leptonic decay rate depends on a different linear combination of g_1 and g_2 ($\approx g_1-\frac{2}{3}\epsilon g_2$), one might hope to use it to further constrain g_2. However, the expected rates for fit 1 and for the $g_2=0$ analysis differ by only 6%. This is not substantially larger than the combined uncertainty in the measured rate and $f_1\sin\theta_C$, so no significant additional constraint is provided.

VIII. CONCLUSIONS

This is the first high-statistics experiment in which all of the $\Sigma^-\rightarrow ne^-\bar{\nu}$ decay products were reconstructed using a polarized Σ^- beam. The control and investigation of systematic errors was greatly facilitated by our ability to reverse the direction of the Σ^- polarization and to orient it in either the horizontal or vertical plane. By simultaneously recording a sample of $\Sigma^-\rightarrow n\pi^-$ events, we were able to use the known value[18] of α_π to determine the Σ^- polarization to be $P=+0.236\pm0.043$ at our 2.5-mrad average production angle. Including both systematic and statistical uncertainties, we determine the decay asymmetry parameters to be $\alpha_e=-0.519\pm0.104$, $\alpha_n=+0.509\pm0.102$, and $\alpha_\nu=-0.230\pm0.061$.

With these values, we have unambiguously established the sign of the axial-vector-to-vector form-factor ratio g_1/f_1 to be negative. This was done by three distinct methods. The first, illustrated in Figs. 16 and 17, relies on the known[18] sign of α_π. The other two methods are independent of the sign of α_π, depending instead on the general vector and axial-vector nature of the decay interaction. This result removes a long-standing disagreement with the Cabibbo model. Also, no evidence is found for a violation of time-reversal invariance in the decay.

From the neutron c.m. energy spectrum, we determine the magnitude of $|g_1/f_1-0.237g_2/f_1|=0.327 \pm 0.007 \pm 0.019$. We assume a dipole form for the q^2 dependence of f_1 and g_1, extracting their ratio at $q^2=0$. Our value is practically insensitive to the value of f_2/f_1 assumed. Making the conventional assumption that $g_2=0$, we get $|g_1(0)/f_1(0)|=-0.327\pm 0.007\pm 0.019$. A general fit which also includes the asymmetry information gives $g_1(0)/f_1(0)=-0.328\pm 0.019$. This result supersedes our preliminary publication[16] where g_1/f_1 was determined from the electron asymmetry parameter. It has a significantly smaller error and is consistent with other recent high-statistics measurements[14,15] (see Table VIII). We note (see Table VII) that a major part of the systematic uncertainty arises from our lack of knowledge of the q^2 dependence. This value is in reasonable agreement with recent fits[3,4,20] of beta-decay data in the baryon octet to the Cabibbo model which give $g_1(0)/f_1(0) = -0.28\pm 0.02$ for $\Sigma^- \rightarrow ne^-\bar{\nu}$.

Using the electron c.m. energy spectrum and the above value of g_1/f_1, we determine the "weak magnetism" form factor, $f_2(0)/f_1(0)=-0.96\pm 0.15$. This value is in agreement with the only other measurement[15] which is $f_2/f_1=-1.02\pm 0.34$. Sirlin[22] has introduced SU(3)-symmetry breaking into the computation of f_2 yielding $f_2/f_1=-0.910\pm 0.034$ which is clearly consistent with our result.

Combining the asymmetry results with the neutron energy spectrum, we have investigated the possibility that g_2 is nonzero. A fit to all of our data (Table X), yields $g_1/f_1=-0.20\pm 0.08$ and $g_2/f_1=+0.56\pm 0.37$. The one- and two-standard-deviation contours which exhibit the strong correlation between g_1 and g_2 are shown in Fig. 22. Our data suggest, but do not compel, a value for g_2/f_1 which has the same (positive) sign as recent bag-model calculations (see Table I) but a larger magnitude. Negative values of g_2/f_1 are clearly disfavored. Because of the strong correlation between g_1 and g_2, a substantial g_2/f_1 would significantly impact g_1/f_1 producing profound effects on the agreement with Cabibbo model. For example, a value of $g_2/f_1 \approx (M_{\Sigma^-}-M_n)/M_{\Sigma^-}$ for $\Sigma^- \rightarrow ne^-\bar{\nu}$ would, in fact, noticeably improve the agreement between experimental results and the Cabibbo model. This is the first experiment which has had sufficient sensitivity to g_2 to investigate these matters.

ACKNOWLEDGMENTS

We thank the staff of Fermilab, particularly the Proton, Physics, and Computing Departments for their assistance. The contributions of A. Krivshich, V. Andreev, C. Patrichev, and G. Garilov to the construction of the TRD chambers and of P. Nevstroev, E. Spiridenkov, and N. Bondaz to the construction of the TRD amplifiers were invaluable. Technical and engineering support from S. Austin, E. Frazier, J. Noh, G. Ridgley, W. Thomas, J. Upton, and R. Wagner is acknowledged. We are grateful to S. Wojcicki for making the neutron calorimeter available to us and to A. Bohm, A. Garcia, and R. J. Oakes for helpful discussions. This work was supported in part by the U.S. Department of Energy under Contracts Nos. DE-AC02-80ER10587, DE-AC02-76CH03000, DE-AC02-76ER03075, and by the U.S.S.R. Academy of Sciences. On of us (S.Y.H.) submitted this work in partial fulfillment of the requirements for a Ph.D. degree in physics at The University of Chicago.

APPENDIX A

In hyperon β decay $Y \rightarrow B + e^- + \bar{\nu}$ the transition rate (T) is given by

$$T=G^2|M|^2(E_B+m_B)/[(2\pi)^5 2m_B(e^{\max}-e)] \times e^2\nu^3 de\, d\Omega_e d\Omega_\nu \ , \qquad (\mathrm{A1})$$

where M is the matrix element, E and m refer to the energy and mass of the baryon, e and ν are the electron and antineutrino energies and $e^{\max}$ is the β spectrum end point. The phase-space factor in Eq. (A1) is already correct to q^2/m^2. We can obtain comparable accuracy in the matrix element by writing[50]

$$M=\langle Be \,|\, H_{\mathrm{eff}} \,|\, Y\nu\rangle \ , \qquad (\mathrm{A2})$$

where H_{eff} operates on two-component spinors and has the structure

$$2\sqrt{2}H_{\mathrm{eff}}=(1-\boldsymbol{\sigma}_l\cdot\mathbf{e})(G_V+G_A\boldsymbol{\sigma}_B\cdot\boldsymbol{\sigma}_l+G_P^e\sigma B\cdot\mathbf{e} + G_P^\nu\boldsymbol{\sigma}_B\cdot\boldsymbol{\nu})(1-\boldsymbol{\sigma}_l\cdot\boldsymbol{\nu}) \ . \qquad (\mathrm{A3})$$

In Eq. (A3) $\mathbf{e}$ and $\boldsymbol{\nu}$ are unit vectors along the electron and antineutrino directions while $\boldsymbol{\sigma}_l$ and $\boldsymbol{\sigma}_B$ operate solely on lepton and baryon states. The effective coupling constants in Eq. (A3) are simple functions of the form factors. In these expressions it is convenient to introduce the small parameter $\Delta=(m_Y-m_B)/m_Y$:

$$\begin{aligned} G_V&=f_1-\Delta f_2+(e+\nu)[f_1+(2-\Delta)f_2]/2m_B \ , \\ G_A&=-g_1+\Delta g_2-(e-\nu)[f_1+(2-\Delta)f_2]/2m_B \ , \qquad (\mathrm{A4}) \\ G_P^e&=e[-f_1+g_1-(2-\Delta)(f_2-g_2)]/2m_B \ , \\ G_P^\nu&=\nu[f_1+g_1+(2-\Delta)(f_2+g_2)]/2m_B \ . \end{aligned}$$

Measurements which average over the leptons, e.g., the rate or the recoil-baryon energy spectrum will be sensitive to G_V, G_A, and $(G_P^e+G_P^\nu)$. In such measurements, we may set terms in $(e-\nu)\approx 0$ and terms in $(e+\nu)/m_B \approx \Delta$. To the same order, we may estimate

$$G_V \approx f_1(1+\Delta/2), \quad G_A \approx -(g_1-\Delta g_2) \ ,$$

$$(G_P^e+G_P^\nu) \approx \Delta(g_1+2g_2)/2 \ .$$

We conclude the following.

(1) The recoil-baryon spectrum will be mainly sensitive to f_1 and the linear combination $g_1-\Delta g_2$ with a slight sensitivity to g_2 separately.

(2) Measurements distinguishing between the leptons, e.g., the electron spectrum will additionally have a first-order sensitivity to the combination (f_1+2f_2) but hardly any sensitivity at all to g_1 and g_2 separately.

APPENDIX B

For a three-body decay such as $\Sigma^-\rightarrow ne^-\bar{\nu}$, the three asymmetry parameters may be evaluated simply as follows: $\alpha_e=2[N(e\uparrow)-N(e\downarrow)]/pN(e\uparrow)+N(e\downarrow)]$ and similarly for the antineutrino and neutron. Here, in an obvious notation, $N(e\uparrow)$ denotes the number of electrons with momenta in the forward hemisphere with respect to the Σ^- polarization, and so forth. These asymmetries are clearly not statistically independent. This may be seen most easily with the aid of Table XI where all events are sorted into one of six exclusive categories.

TABLE XI. Six exclusive categories for $\Sigma^-\rightarrow ne^-\bar{\nu}$ decay product configurations. Note that the remaining two categories ↑↑↑ and ↓↓↓ are forbidden by momentum conservation.

Category	e	$\bar{\nu}$	n
1	↑	↑	↓
2	↓	↓	↑
3	↑	↓	↑
4	↓	↑	↓
5	↓	↑	↑
6	↑	↓	↓

One then readily finds the following relations:

$$\alpha_e=2[(N_1+N_3+N_6)-(N_2+N_4+N_5)]/N\ ,$$

$$\alpha_\nu=2[(N_1+N_4+N_5)-(N_2+N_3+N_6)]/N\ ,$$

$$\alpha_n=2[(N_2+N_3+N_5)-(N_1+N_4+N_6)]/N\ .$$

Here N_i denotes the number of events in the ith category and $N=\sum_{i=1}^{6}N_i$ is the total number of events. Since the α parameters have some N_i in common, it is evident that they are not statistically independent.

However, the pairwise sums

$$\alpha_e+\alpha_\nu=4(N_1-N_2)/N\ ,$$

$$\alpha_e+\alpha_n=4(N_3-N_4)/N\ ,$$

$$\alpha_\nu+\alpha_n=4(N_5-N_6)/N$$

have no N_i in common. They are therefore statistically independent in so far as we may neglect fluctuations in the total number of events N.

---

[*] Present address: Fermilab, Batavia, Illinois 60510.

[†] Present address: Stanford Linear Accelerator Center, Stanford, California 94305.

[‡] Present address: Supercomputer Research Center, Institute for Defense Analyses, Lanham, Maryland 20706.

[§] Present address: E. P. Division, CERN, CH-1211 Geneva 23, Switzerland.

[**] Present address: Brookhaven National Laboratory, Upton, New York 11973.

[††] Permanent address: H. H. Wills Physics Laboratory, University of Bristol, Bristol BS8 1TL, England.

[‡‡] Present address: Eidg. Technische Hochschule, Zurich, Switzerland.

[§§] Present address: Mitre Corporation, Bedford, Massachusetts 01730.

[1] N. Cabibbo, Phys. Rev. Lett. **10**, 531 (1963). See also Z. Maki, M. Nakagawa, and S. Sakata, in *Proceedings of the 1962 International Conference on High Energy Physics,* edited by J. Prentki (CERN, Geneva, 1962), p. 663; M. Gell-Mann and M. Levy, Nuovo Cimento **16**, 705 (1960).

[2] N. Cabibbo and F. Chilton, Phys. Rev. **137B**, 1628 (1965).

[3] J.-M. Gaillard and G. Sauvage, Annu. Rev. Nucl. Part. Sci. **34**, 351 (1985).

[4] A. Bohm and M. Kmiecik, Phys. Rev. D **31**, 3005 (1985).

[5] P. Keller *et al.*, Phys. Rev. Lett. **48**, 971 (1982).

[6] R. J. Ellis *et al.*, Nucl. Phys. **B29**, 77 (1982).

[7] D. Bogert *et al.*, Phys. Rev. D **2**, 6 (1970).

[8] L. K. Gershwin *et al.*, Phys. Rev. Lett. **20**, 1270 (1968); L. K. Gershwin, Ph.D. thesis, University of California, 1969. The results presented in the latter should be used: R. Tripp (private communication).

[9] A. Garcia and E. C. Swallow, Phys. Rev. Lett. **35**, 467 (1975).

[10] D. Decamp *et al.*, Phys. Lett. **66B**, 295 (1977).

[11] A. P. Colleraine *et al.*, Phys. Rev. Lett. **23**, 198 (1969).

[12] F. Eisele *et al.*, Z. Phys. **223**, 487 (1969).

[13] C. Baltay *et al.*, Phys. Rev. D **5**, 1569 (1972).

[14] W. Tanenbaum *et al.*, Phys. Rev. D **12**, 1871 (1975).

[15] M. Bourquin *et al.*, Z. Phys. C **21**, 17 (1983).

[16] S. Y. Hsueh *et al.*, Phys. Rev. Lett. **54**, 2399 (1985).

[17] A. Garcia and P. Kielanowski, *The Beta Decay of Hyperons,* (Lecture Notes in Physics, Vol. 222) (Springer, Berlin, 1985). Our sign convention is such that g_1/f_1 is positive for neutron decay.

[18] Particle Data Group, M. Aguilar-Benitez *et al.*, Phys. Lett. **107B**, 1 (1986). Note that our sign convention for the form-factor ratios is different from that used by the Particle Data Group, and that they quote the neutron asymmetry for $\Sigma^-\rightarrow n\pi^-$ which is $-\alpha_\pi$.

[19] A variety of values for f_2/f_1 in the SU(3) limit can be found in the literature corresponding to different ways of handling the normalizing mass for f_2. This ambiguity is a direct reflection of the fact that f_2 is subject to first-order symmetry-breaking corrections. Though our notation is slightly different, we follow the approach used by Sirlin in Ref. 22.

[20] M. Bourquin *et al.*, Z. Phys. C **21**, 27 (1983).

[21] M. Ademollo and R. Gatto, Phys. Rev. Lett. **13**, 264 (1964).

[22] A. Sirlin, Nucl. Phys. **B161**, 301 (1979).

[23] G. Zapalec *et al.*, Phys. Rev. Lett. **57**, 1526 (1986).

[24] For a recent review, see L. J. Carson, R. J. Oakes, and C. R. Willcox, Phys. Rev. D **37**, 3197 (1988).

[25] K. Ushio, Z. Phys. C **30**, 115 (1986).

[26] L. J. Carson, R. J. Oakes, and C. R. Willcox, Phys. Lett. **164B**, 155 (1985).

[27] L. J. Carson, R. J. Oakes, and C. R. Willcox, Phys. Rev. D **33**, 1356 (1986).

[28] A. Halperin, B. W. Lee, and P. Sorba, Phys. Rev. D **14**, 2343 (1976).

[29] J. F. Donoghue and R. Holstein, Phys. Rev. D **25**, 206 (1982).

[30] K. Kubodera, Y. Kohyama, K. Oikawa, and C. W. Kim, Nucl. Phys. **A439**, 695 (1985).

[31] Ø. Lie-Svendsen and H. Høgaasen, Z. Phys. C **35**, 239 (1987); J. Ø. Eeg, H. Høgaasen, and Ø. Lie-Svendsen, *ibid.* **31**, 443 (1986).

[32] Our sign convention is such that q^2 is positive in decay processes. Note that normal pole-type form factors rise in the decay region as q^2 increases.

[33] D. R. Harrington, Phys. Rev. **120**, 1482 (1960).

[34] I. Bender, V. Linke, and H. J. Rothe, Z. Phys. **212**, 190 (1968).

[35] V. Linke, Nucl. Phys. **B12**, 669 (1969).

[36] K. Töth, T. Margaritisz, and K. Szegö, CERN Report No. TH 3169, 1981 (unpublished).

[37] K. Töth, T. Margaritisz, and K. Szegö, Phys. Rev. D **33**, 3306 (1986).

[38] T. R. Cardello *et al.*, Phys. Rev. D **32**, 1 (1985).

[39] W. Frieze *et al.*, Nucl. Instrum. Methods **135**, 93 (1976).

[40] A. V. Kulikov *et al.*, in *Proceedings of the Santa Fe Meeting,* Annual Meeting of the Division of Particles and Fields of the APS, Santa Fe, New Mexico, 1984, edited by T. Goldmand and M. M. Nieto (World Scientific, Singapore, 1985), p. 358.

[41] V. A. Andreev *et al.*, Leningrad Nuclear Physics Institute Report No. 1186, 1986 (unpublished).

[42] C. W. Fabjan *et al.*, Nucl. Instrum. Methods **185**, 119 (1981).

[43] J. A. Appel *et al.*, Nucl. Instrum. Methods **127**, 495 (1975).

[44] Modified from the calorimeter described in J. P. Dishaw, Ph.D. thesis, Stanford Linear Accelerator Center, Report No. SLAC-216, UC-34d, 1979.

[45] Y. S. Tsai, Rev. Mod. Phys. **46**, 815 (1974). We used formulas (4.7).

[46] B. Rossi, *High Energy Particles* (Prentice-Hall, Englewood Cliffs, NJ, 1961).

[47] R. Oehme, E. Swallow, and R. Winston, Phys. Rev. D **8**, 2124 (1973).

[48] J. D. Jackson, S. B. Trieman, and H. W. Wyld, Phys. Rev. **106**, 517 (1957).

[49] P. Razis, Ph.D. thesis, Yale University, 1986.

[50] J. M. Watson and R. Winston, Phys. Rev. **181**, 1907 (1969).

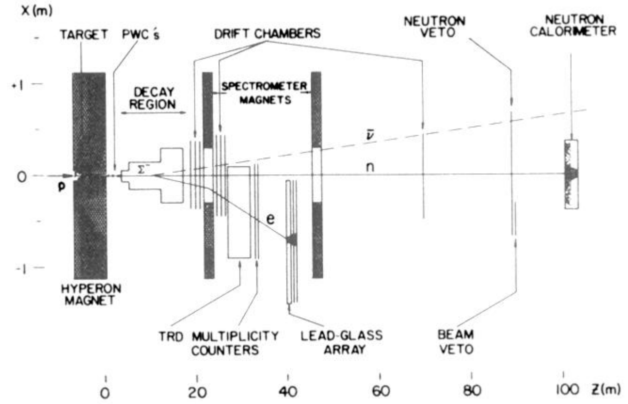

FIG. 1. Plan view of the experimental apparatus.

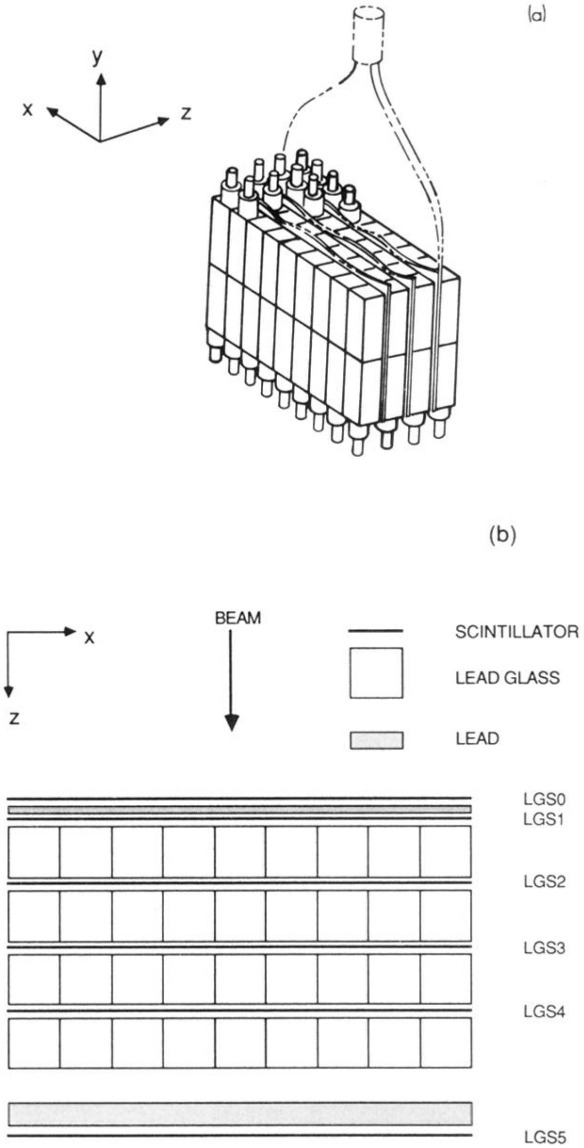

FIG. 4. The lead-glass calorimeter (LGC). (a) The glass blocks were configured in four layers in the *z* direction counters between the layers. (b) The top view showing the longitudinal geometry of lead, glass, and scintillators. The media type is indicated in upper-right corner.